1-1-2001

Measurement of the Neutral Current Cross Section and F_2 Structure Function for Deep Inelastic e^+p Scattering at HERA

S. Chekanov
Argonne National Laboratory

M. Derrick
Argonne National Laboratory

D. Krakauer
Argonne National Laboratory

S. Magill
Argonne National Laboratory

B. Musgrave
Argonne National Laboratory

Eur. Phys. J. C 21, 443–471 (2001)
Digital Object Identifier (DOI) 10.1007/s100520100749

THE EUROPEAN PHYSICAL JOURNAL C

Measurement of the neutral current cross section and F_2 structure function for deep inelastic e^+p scattering at HERA

The ZEUS Collaboration

S. Chekanov, M. Derrick, D. Krakauer, S. Magill, B. Musgrave, A. Pellegrino, J. Repond, R. Stanek, R. Yoshida
Argonne National Laboratory, Argonne, IL, USA[p]

M.C.K. Mattingly
Andrews University, Berrien Springs, MI, USA

P. Antonioli, G. Bari, M. Basile, L. Bellagamba, D. Boscherini[1], A. Bruni, G. Bruni, G. Cara Romeo, L. Cifarelli[2], F. Cindolo, A. Contin, M. Corradi, S. De Pasquale, P. Giusti, G. Iacobucci, G. Levi, A. Margotti, T. Massam, R. Nania, F. Palmonari, A. Pesci, G. Sartorelli, A. Zichichi
University and INFN Bologna, Bologna, Italy[f]

G. Aghuzumtsyan, I. Brock, R. Deffner[3], S. Goers, H. Hartmann, E. Hilger, P. Irrgang, H.-P. Jakob, A. Kappes[4], U.F. Katz[5], R. Kerger, O. Kind, E. Paul, J. Rautenberg, H. Schnurbusch, A. Stifutkin, J. Tandler, K.C. Voss, A. Weber, H. Wieber
Physikalisches Institut der Universität Bonn, Bonn, Germany[c]

D.S. Bailey[6], N.H. Brook[6], J.E. Cole, B. Foster, G.P. Heath, H.F. Heath, S. Robins, E. Rodrigues[7], J. Scott, R.J. Tapper, M. Wing
H.H. Wills Physics Laboratory, University of Bristol, Bristol, UK[o]

M. Capua, A. Mastroberardino, M. Schioppa, G. Susinno
Calabria University, Physics Dept.and INFN, Cosenza, Italy[f]

H.Y. Jeoung, J.Y. Kim, J.H. Lee, I.T. Lim, K.J. Ma, M.Y. Pac[8]
Chonnam National University, Kwangju, Korea[h]

A. Caldwell, M. Helbich, W. Liu, X. Liu, B. Mellado, S. Paganis, S. Sampson, W.B. Schmidke, F. Sciulli
Columbia University, Nevis Labs., Irvington on Hudson, NY, USA[q]

J. Chwastowski, A. Eskreys, J. Figiel, K. Klimek[9], K. Olkiewicz, M.B. Przybycień[10], P. Stopa, L. Zawiejski
Inst. of Nuclear Physics, Cracow, Poland[j]

B. Bednarek, K. Jeleń, D. Kisielewska, A.M. Kowal[11], M. Kowal, T. Kowalski, B. Mindur, M. Przybycień, E. Rulikowska-Zarębska, L. Suszycki, D. Szuba
Faculty of Physics and Nuclear Techniques, Academy of Mining and Metallurgy, Cracow, Poland[j]

A. Kotański
Jagellonian Univ., Dept. of Physics, Cracow, Poland

L.A.T. Bauerdick[12], U. Behrens, K. Borras, V. Chiochia, J. Crittenden[13], D. Dannheim, K. Desler, G. Drews, A. Fox-Murphy, U. Fricke, A. Geiser, F. Goebel, P. Göttlicher, R. Graciani, T. Haas, W. Hain, G.F. Hartner, K. Hebbel, S. Hillert, W. Koch[14,†], U. Kötz, H. Kowalski, H. Labes, B. Löhr, R. Mankel, J. Martens, M. Martínez, M. Milite, M. Moritz, D. Notz, M.C. Petrucci, A. Polini, U. Schneekloth, F. Selonke, S. Stonjek, G. Wolf, U. Wollmer, J.J. Whitmore[15], R. Wichmann[16], C. Youngman, W. Zeuner
Deutsches Elektronen-Synchrotron DESY, Hamburg, Germany

C. Coldewey, A. Lopez-Duran Viani, A. Meyer, S. Schlenstedt
DESY Zeuthen, Zeuthen, Germany

G. Barbagli, E. Gallo, P. G. Pelfer
University and INFN, Florence, Italy[f]

A. Bamberger, A. Benen, N. Coppola, P. Markun, H. Raach[17], S. Wölfle
Fakultät für Physik der Universität Freiburg i.Br., Freiburg i.Br., Germany[c]

M. Bell, P.J. Bussey, A.T. Doyle, C. Glasman, S.W. Lee[18], A. Lupi, G.J. McCance, D.H. Saxon, I.O. Skillicorn
Dept. of Physics and Astronomy, University of Glasgow, Glasgow, UK[o]

B. Bodmann, N. Gendner, U. Holm, H. Salehi, K. Wick, A. Yildirim, A. Ziegler
Hamburg University, I. Institute of Exp. Physics, Hamburg, Germany[c]

T. Carli, A. Garfagnini, I. Gialas[19], E. Lohrmann
Hamburg University, II. Institute of Exp. Physics, Hamburg, Germany[c]

C. Foudas, R. Gonçalo[7], K.R. Long, F. Metlica, D.B. Miller, A.D. Tapper, R. Walker
Imperial College London, High Energy Nuclear Physics Group, London, UK[o]

P. Cloth, D. Filges
Forschungszentrum Jülich, Institut für Kernphysik, Jülich, Germany

M. Kuze, K. Nagano, K. Tokushuku[20], S. Yamada, Y. Yamazaki
Institute of Particle and Nuclear Studies, KEK, Tsukuba, Japan[g]

A.N. Barakbaev, E.G. Boos, N.S. Pokrovskiy, B.O. Zhautykov
Institute of Physics and Technology of Ministry of Education and Science of Kazakhstan, Almaty, Kazakhstan

S.H. Ahn, S.B. Lee, S.K. Park
Korea University, Seoul, Korea[h]

H. Lim[18], D. Son
Kyungpook National University, Taegu, Korea[h]

F. Barreiro, G. García, O. González, L. Labarga, J. del Peso, I. Redondo[21], J. Terrón, M. Vázquez
Univer. Autónoma Madrid, Depto de Física Teórica, Madrid, Spain[n]

M. Barbi, F. Corriveau, A. Ochs, S. Padhi, D.G. Stairs
McGill University, Dept. of Physics, Montréal, Québec, Canada[a], [b]

T. Tsurugai
Meiji Gakuin University, Faculty of General Education, Yokohama, Japan

A. Antonov, V. Bashkirov[22], P. Danilov, B.A. Dolgoshein, D. Gladkov, V. Sosnovtsev, S. Suchkov
Moscow Engineering Physics Institute, Moscow, Russia[l]

R.K. Dementiev, P.F. Ermolov, Yu.A. Golubkov, I.I. Katkov, L.A. Khein, N.A. Korotkova, I.A. Korzhavina, V.A. Kuzmin, B.B. Levchenko, O.Yu. Lukina, A.S. Proskuryakov, L.M. Shcheglova, A.N. Solomin, N.N. Vlasov, S.A. Zotkin
Moscow State University, Institute of Nuclear Physics, Moscow, Russia[m]

C. Bokel, J. Engelen, S. Grijpink, E. Maddox, E. Koffeman, P. Kooijman, S. Schagen, E. Tassi, H. Tiecke, N. Tuning, J.J. Velthuis, L. Wiggers, E. de Wolf
NIKHEF and University of Amsterdam, Amsterdam, The Netherlands[i]

N. Brümmer, B. Bylsma, L.S. Durkin, J. Gilmore, C.M. Ginsburg, C.L. Kim, T.Y. Ling
Ohio State University, Physics Department, Columbus, OH, USA[p]

S. Boogert, A.M. Cooper-Sarkar, R.C.E. Devenish, J. Ferrando, J. Große-Knetter[23], T. Matsushita, A. Quadt[23], M. Rigby, O. Ruske, M.R. Sutton, R. Walczak
Department of Physics, University of Oxford, Oxford UK[o]

A. Bertolin, R. Brugnera, R. Carlin, F. Dal Corso, S. Dusini, S. Limentani, A. Longhin, A. Parenti, M. Posocco, L. Stanco, M. Turcato
Dipartimento di Fisica dell' Università and INFN, Padova, Italy[f]

L. Adamczyk[24], L. Iannotti[24], B.Y. Oh, P.R.B. Saull[24], W.S. Toothacker[14,†]
Pennsylvania State University, Dept. of Physics, University Park, PA, USA[q]

Y. Iga
Polytechnic University, Sagamihara, Japan[g]

G. D'Agostini, G. Marini, A. Nigro
Dipartimento di Fisica, Univ. 'La Sapienza' and INFN, Rome, Italy[f]

C. Cormack, J.C. Hart, N.A. McCubbin
Rutherford Appleton Laboratory, Chilton, Didcot, Oxon, UK[o]

D. Epperson, C. Heusch, H.F.-W. Sadrozinski, A. Seiden, D.C. Williams
University of California, Santa Cruz, CA, USA[p]

I.H. Park
Seoul National University, Seoul, Korea

N. Pavel
Fachbereich Physik der Universität-Gesamthochschule Siegen, Germany[c]

H. Abramowicz, S. Dagan, A. Gabareen, S. Kananov, A. Kreisel, A. Levy
Raymond and Beverly Sackler Faculty of Exact Sciences, School of Physics, Tel-Aviv University, Tel-Aviv, Israel[e]

T. Abe, T. Fusayasu, T. Kohno, K. Umemori, T. Yamashita
Department of Physics, University of Tokyo, Tokyo, Japan[g]

R. Hamatsu, T. Hirose, M. Inuzuka, S. Kitamura[25], K. Matsuzawa, T. Nishimura
Tokyo Metropolitan University, Dept. of Physics, Tokyo, Japan[g]

M. Arneodo[26], N. Cartiglia, R. Cirio, M. Costa, M.I. Ferrero, S. Maselli, V. Monaco, C. Peroni, M. Ruspa, R. Sacchi, A. Solano, A. Staiano
Università di Torino, Dipartimento di Fisica Sperimentale and INFN, Torino, Italy[f]

D.C. Bailey, C.-P. Fagerstroem, R. Galea, T. Koop, G.M. Levman, J.F. Martin, A. Mirea, A. Sabetfakhri
University of Toronto, Dept. of Physics, Toronto, Ont., Canada[a]

J.M. Butterworth, C. Gwenlan, R. Hall-Wilton, M.E. Hayes, E.A. Heaphy, T.W. Jones, J.B. Lane, B.J. West
University College London, Physics and Astronomy Dept., London, UK[o]

J. Ciborowski[27], R. Ciesielski, G. Grzelak, R.J. Nowak, J.M. Pawlak, B. Smalska[28], T. Tymieniecka, J. Ukleja, J.A. Zakrzewski, A.F. Żarnecki
Warsaw University, Institute of Experimental Physics, Warsaw, Poland[j]

M. Adamus, P. Plucinski, J. Sztuk
Institute for Nuclear Studies, Warsaw, Poland[j]

O. Deppe[29], Y. Eisenberg, L.K. Gladilin[30], D. Hochman, U. Karshon
Weizmann Institute, Department of Particle Physics, Rehovot, Israel[d]

J. Breitweg, D. Chapin, R. Cross, D. Kçira, S. Lammers, D.D. Reeder, A.A. Savin, W.H. Smith, M. Wodarczyk[31]
University of Wisconsin, Dept. of Physics, Madison, WI, USA[p]

A. Deshpande, S. Dhawan, V.W. Hughes P.B. Straub
Yale University, Department of Physics, New Haven, CT, USA[p]

S. Bhadra, C.D. Catterall, W.R. Frisken, M. Khakzad, S. Menary
York University, Dept. of Physics, Toronto, Ont., Canada[a]

[1] now visiting scientist at DESY
[2] now at Univ. of Salerno and INFN Napoli, Italy
[3] now at Siemens ICN, Berlin, Germany
[4] supported by the Fig, contract I-523-13.7/97
[5] on leave of absence at University of Erlangen-Nürnberg, Germany

[6] PPARC Advanced fellow
[7] supported by the Portuguese Foundation for Science and Technology (FCT)
[8] now at Dongshin University, Naju, Korea
[9] supported by the Polish State Committee for Scientific Research grant no. 5 P-03B 08720
[10] now at Northwestern Univ., Evaston/IL, USA
[11] supported by the Polish State Committee for Scientific Research grant no. 5 P-03B 13720
[12] now at Fermilab, Batavia/IL, USA
[13] on leave of absence from Bonn University
[14] deceased
[15] on leave from Penn State University, USA
[16] partly supported by Penn State University and Fig, contract I-523-013.07/97
[17] supported by DESY
[18] partly supported by an ICSC-World Laboratory Björn H. Wiik Scholarship
[19] Univ. of the Aegean, Greece
[20] also at University of Tokyo
[21] supported by the Comunidad Autonoma de Madrid
[22] now at Loma Linda University, Loma Linda, CA, USA
[23] now at CERN, Geneva, Switzerland
[24] partly supported by Tel Aviv University
[25] present address: Tokyo Metropolitan University of Health Sciences, Tokyo 116-8551, Japan
[26] now also at Università del Piemonte Orientale, 28100 Novara, Italy
[27] and Łódź University, Poland
[28] supported by the Polish State Committee for Scientific Research, grant no. 2P03B 002 19
[29] now at EVOTEC BioSystems AG, Hamburg, Germany
[30] on leave from MSU, partly supported by University of Wisconsin via the U.S.-Israel BSF
[31] now at Intel, Portland/Oregon, USA

Received: 30 May 2001 /
Published online: 24 August 2001 –

Abstract. The cross section and the proton structure function F_2 for neutral current deep inelastic e^+p scattering have been measured with the ZEUS detector at HERA using an integrated luminosity of 30 pb^{-1}. The data were collected in 1996 and 1997 at a centre-of-mass energy of 300 GeV. They cover the kinematic range $2.7 < Q^2 < 30000$ GeV^2 and $6 \cdot 10^{-5} < x < 0.65$. The variation of F_2 with x and Q^2 is well described by next-to-leading-order perturbative QCD as implemented in the DGLAP evolution equations.

1 Introduction

The measurements of the differential cross-section and F_2 structure function in neutral current (NC) deep inelastic scattering (DIS) at HERA have been vital in testing the predictions of perturbative QCD and in the determination of the parton densities in the proton at low x. In both of these areas of study the accuracy and precision of the measurements are of paramount importance.

[a] supported by the Natural Sciences and Engineering Research Council of Canada (NSERC)
[b] supported by the FCAR of Québec, Canada
[c] supported by the German Federal Ministry for Education and Science, Research and Technology (BMBF), under contract numbers 057BN19P, 057FR19P, 057HH19P, 057HH29P, 057SI75I
[d] supported by the MINERVA Gesellschaft für Forschung GmbH, the Israel Science Foundation, the U.S.-Israel Binational Science Foundation, the Israel Ministry of Science and the Benozyio Center for High Energy Physics
[e] supported by the German-Israeli Foundation, the Israel Science Foundation, and by the Israel Ministry of Science
[f] supported by the Italian National Institute for Nuclear Physics (INFN)
[g] supported by the Japanese Ministry of Education, Science and Culture (the Monbusho) and its grants for Scientific Research
[h] supported by the Korean Ministry of Education and Korea Science and Engineering Foundation
[i] supported by the Netherlands Foundation for Research on Matter (FOM)
[j] supported by the Polish State Committee for Scientific Research, grant no. 2P03B04616, 620/E-77/SPUB-M/DESY/P-03/DZ 247/2000 and 112/E-356/SPUB-M/DESY/P-03/DZ 3001/2000
[l] partially supported by the German Federal Ministry for Education and Science, Research and Technology (BMBF)
[m] supported by the Fund for Fundamental Research of Russian Ministry for Science and Education and by the German Federal Ministry for Education and Science, Research and Technology (BMBF)
[n] supported by the Spanish Ministry of Education and Science through funds provided by CICYT
[o] supported by the Particle Physics and Astronomy Research Council, UK
[p] supported by the US Department of Energy
[q] supported by the US National Science Foundation

The measurements of the double-differential cross-section $\mathrm{d}\sigma^{ep}/\mathrm{d}x\mathrm{d}Q^2$ and F_2^{em} presented here are based on an e^+p DIS event sample twelve times larger than that used in the previous ZEUS publication [1]. This increase, combined with an improved understanding of the detector, results in a significant decrease in both the statistical and systematic uncertainties[1]. The uncertainties are systematics dominated for $Q^2 < 800$ GeV^2.

The outline of the paper is as follows: in Sect. 2, the kinematics and the cross section of e^+p NC DIS are discussed; in Sects. 3 and 4, the experimental conditions and the trigger used in the data taking are presented; Sect. 5 explains the method of the reconstruction of the kinematic variables; in Sect. 6, Monte Carlo simulations used in the analyses are described; Sects. 7 and 8 discuss the details of the basic measured quantities; in Sect. 9, the characteristics of the selected events are examined; Sect. 10 presents the results; and Sect. 11 contains the conclusions.

2 Kinematics and cross section

The kinematics of deep inelastic scattering, $e(k)+p(P) \to e(k')+X$, can be completely described by the negative of the four-momentum-transfer squared, Q^2, and Bjorken x. In the absence of QED radiation,

$$Q^2 = -q^2 = -(k-k')^2,$$
$$x = \frac{Q^2}{2P\cdot q},$$

where k and P are the four-momenta of the incoming particles and k' is the four-momentum of the scattered lepton. The fraction of the lepton energy transferred to the proton in its rest frame is $y = (P\cdot q)/(P\cdot k) = Q^2/(sx)$, where s is the square of the total centre-of-mass energy of the lepton-proton collision. The invariant mass of the hadronic final state, W, is calculated from

$$W^2 = Q^2\frac{1-x}{x} + m_p^2,$$

where m_p is the proton mass.

The double-differential cross section for inclusive e^+p scattering is given in terms of the structure functions F_i:

$$\frac{d^2\sigma^{e^+p}}{dx\,dQ^2} = \frac{2\pi\alpha^2}{xQ^4}\Big[Y_+F_2(x,Q^2) - Y_-xF_3(x,Q^2) - y^2F_L(x,Q^2)\Big](1+\delta_r(x,Q^2)) \quad (1)$$
$$= \frac{d^2\sigma^{e^+p}_{\mathrm{Born}}}{dx\,dQ^2}(1+\delta_r(x,Q^2)),$$

where $Y_\pm = 1\pm(1-y)^2$ and x and Q^2 are defined at the hadronic vertex. In this equation, F_L is the longitudinal structure function, xF_3 is the parity-violating term arising from Z^0 exchange and δ_r is the electroweak radiative correction. The double-differential Born cross section, $d^2\sigma_{\mathrm{Born}}/dxdQ^2$, is evaluated using $1/\alpha = 137.03599$, $\sin^2\theta_W = 0.23147$ and $M_Z = 91.1882$ GeV [4] to determine the electroweak parameters [5].

The structure function F_2 contains contributions from both virtual photon and Z^0 exchange:

$$F_2 = F_2^{em} + \frac{Q^2}{(Q^2+M_Z^2)}F_2^{int} + \frac{Q^4}{(Q^2+M_Z^2)^2}F_2^{wk}$$
$$= F_2^{em}(1+\Delta_{F_2}), \quad (2)$$

where M_Z is the mass of the Z^0 and the contributions to F_2 from photon exchange (F_2^{em}), Z^0 exchange (F_2^{wk}) and the $Z^0-\gamma$ interference term (F_2^{int}) are indicated separately. All three contributions are included in the reduced cross section, $\tilde{\sigma}^{e^+p}$, defined as:

$$\tilde{\sigma}^{e^+p} = \left[\frac{2\pi\alpha^2}{xQ^4}Y_+\right]^{-1}\frac{d^2\sigma^{e^+p}_{\mathrm{Born}}}{dx\,dQ^2}.$$

3 Experimental conditions

The data presented here were taken in 1996 and 1997 using the ZEUS detector at HERA. In this period HERA operated with 174-177 bunches of 820 GeV protons and 27.5 GeV positrons, which collided every 96 ns. Additional unpaired positron, unpaired proton and empty bunches were used to determine beam-related backgrounds. The proton bunch length was approximately 11 cm (r.m.s.) while the positron bunch length was negligible in comparison. Variations of the mean interaction position (from run to run) lead to an effective length of the interaction region of 11.5 cm (r.m.s.) centred[2] around $Z = -0.5$ cm. Approximately 6% of the proton current was contained in satellite bunches, which were shifted by ± 4.8 ns with respect to the nominal bunch crossing time, resulting in a fraction of the ep interactions occurring at $\langle Z\rangle \simeq \pm 72$ cm.

A brief outline of the components which are most relevant for this analysis, as illustrated in Fig. 1, is given below. The uranium-scintillator calorimeter (CAL) [6] covers 99.7% of the total solid angle. It consists of the barrel calorimeter (BCAL), covering the polar angle range $36.7^\circ < \theta < 129.1^\circ$, the forward calorimeter (FCAL), covering $2.6^\circ < \theta < 36.7^\circ$ and the rear calorimeter (RCAL), covering $129.1^\circ < \theta < 178.5^\circ$. The FCAL and RCAL are divided vertically into two halves to allow temporary retraction during beam injection. The CAL is segmented into electromagnetic (EMC) and hadronic (HAC) sections. Each section is further subdivided into cells of typically 5×20 cm^2 (10×20 cm^2 in the RCAL) for the

[1] Data on F_2^{em} based on similar statistics and in a similar kinematic range have recently been presented by the H1 collaboration [2,3]

[2] The ZEUS coordinate system is a right-handed Cartesian system, with the Z axis pointing in the proton beam direction, referred to as the "forward direction", and the X axis pointing left towards the centre of HERA. The coordinate origin is at the nominal interaction point

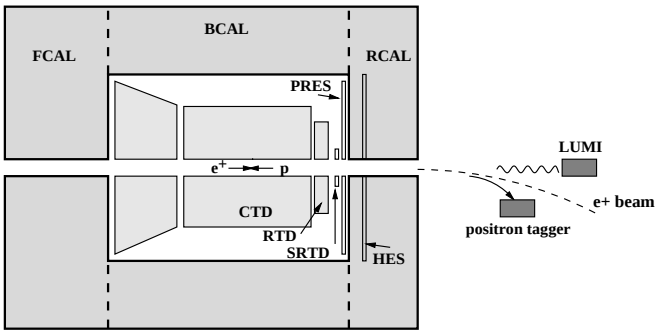

Fig. 1. Schematic view of the ZEUS detector showing those components important for this analysis

EMC and 20×20 cm^2 for the HAC sections. Each cell is viewed by two photomultiplier tubes (PMTs). Under test-beam conditions, the calorimeter has a single particle energy resolution of $\sigma/E = 18\%/\sqrt{E(\mathrm{GeV})}$ for electrons and $\sigma/E = 35\%/\sqrt{E(\mathrm{GeV})}$ for hadrons [6]. The timing resolution of a calorimeter cell is better than 1 ns for energy deposits greater than 4.5 GeV. To minimise the effects of noise coming from the uranium radioactivity, all EMC (HAC) cells with an energy deposit of less than 60 (110) MeV were discarded in the analysis. For the remaining cells with no neighbouring energy deposits, this cut was increased to 100 (160) MeV.

A presampler (PRES) [7] is mounted in front of FCAL and RCAL. It consists of scintillator tiles that detect particles originating from showers in the material between the interaction point and the calorimeter. This information is used to correct the energy of the scattered positron.

The tracking system consists of a central tracking chamber (CTD) [8] and a rear tracking detector (RTD) [9] enclosed in a 1.43 T solenoidal magnetic field. The interaction vertex was measured with a typical resolution along (transverse to) the beam direction of 0.4 (0.1) cm. The CTD was used to measure track momenta with a resolution of $\sigma(p_t)/p_t = 0.0058p_t \oplus 0.0065 \oplus 0.0014/p_t$ (p_t in GeV) and to extrapolate tracks onto the face of the calorimeter with a resolution of 0.3 cm.

The position of positrons scattered at small angles to the positron-beam direction was measured using the small-angle rear tracking detector (SRTD) [10], which is attached to the front face of the RCAL. The SRTD consists of two planes of scintillator strips, 1 cm wide and 0.5 cm thick, arranged in orthogonal directions and read out via optical fibres and photomultiplier tubes. It covers the region of about 68×68 cm^2 in X and Y and is positioned at $Z = -148$ cm. A hole of 8×20 cm^2 at the centre of the RCAL and SRTD accommodates the beampipe. The SRTD signals resolve single minimum-ionising particles and provide a transverse position resolution of 3 mm. The time resolution is better than 2 ns for a minimum-ionising particle. The RTD was used to determine accurately the position of the SRTD.

The hadron-electron separator (HES) [9] consists of a layer of silicon pad detectors. The rear HES is located in the RCAL at a depth of 3.3 radiation lengths. Each silicon pad has an area of 28.9×30.5 mm^2, providing a spatial resolution of about 9 mm for a single hit pad. If more than one adjacent pad is hit by a shower, a cluster consisting of at most 3×3 pads around the most energetic pad is considered, giving a positron position resolution of 5 mm.

The luminosity was measured via the bremsstrahlung process, $ep \to e\gamma p$, using a lead-scintillator calorimeter (LUMI) [11] which detects photons at angles ≤ 0.5 mrad with respect to the positron beam direction. The LUMI photon calorimeter was also used to tag photons from initial-state radiation in DIS events. It was positioned at $Z = -107$ m and had an intrinsic energy resolution of $\sigma/E = 18\%/\sqrt{E(\mathrm{GeV})}$. The carbon-lead filter, placed in front of the calorimeter to shield it from synchrotron radiation, degraded its energy resolution somewhat. The position resolution was 0.2 cm in X and Y. In addition, an electromagnetic calorimeter (positron tagger) positioned at $Z = -35$ m was used for tagging positrons scattered at very small angles.

4 Trigger

For the 'high-Q^2 region' ($Q^2 \geq 30$ GeV^2), the data analysed correspond to an integrated luminosity of 30.6 ± 0.5 pb^{-1}. For the 'low-Q^2 region' ($Q^2 \geq 2$ GeV^2), where the positrons are scattered through smaller angles, the data set corresponds to an integrated luminosity of 2.23 ± 0.02 pb^{-1}, which was obtained in short dedicated running periods.

Events were selected online by a three-level trigger system [9]. At the first level (FLT) [12], events with a positron candidate were selected by the logical OR of the following conditions:

- total EMC energy deposit in the BCAL greater than 4.8 GeV;
- total EMC energy deposit in the RCAL, excluding the ring of 20×20 cm^2 towers closest to the rear beampipe, greater than 3.4 GeV;
- an isolated positron condition (ISO-e) in the RCAL. The ISO-e condition requires that the isolated EMC energy deposit be greater than 2.08 GeV and that the HAC energy behind it be either less than 0.95 GeV or no more than one third of the EMC energy. The isolation criterion required all towers adjacent to the EMC energy deposit associated with the positron to have energy deposits less than 2.08 GeV in the EMC and 0.95 GeV in the HAC. Additionally, the total energy deposit in CAL was required to be greater than 0.464 GeV and a signal above threshold was required in the SRTD;
- total transverse energy in the CAL greater than 30 GeV;
- total transverse energy in the CAL greater than 11.6 GeV and at least one track candidate in the CTD;
- total EMC energy deposit in the CAL greater than 10 GeV and at least one track candidate in the CTD.

Backgrounds from protons interacting outside the detector were rejected using the time measurement of the energy deposits in upstream veto counters and in the SRTD.

The trigger efficiency of the FLT for events that passed the offline selection cuts (see Sect. 9.1) was greater than 99%, as determined from dedicated trigger studies and from Monte Carlo (MC) simulations.

The second-level trigger (SLT) further reduced the background using the times measured in the calorimeter cells and the summed energies from the calorimeter. Energy and momentum conservation require ep-collisions to conserve δ:

$$\delta = E - P_Z = \sum_i E_i(1 - \cos\theta_i). \tag{3}$$

In this equation, E_i and θ_i are the energies and polar angles of all energy deposits in the CAL. For perfect detector resolution and for fully contained DIS events, δ will equal twice the positron beam energy (55 GeV). For photoproduction events, where the scattered positron escapes down the beampipe, δ peaks at much lower values. Proton beam-gas events that originate from inside the detector have energy concentrated in the forward direction and so also have small values of δ.

The events were accepted at the SLT if they satisfied the condition that

$$\delta_{SLT} = \sum_i E_i(1 - \cos\vartheta_i) > (29\ \text{GeV} - 2E_\gamma)$$

where ϑ_i is the polar angle of the energy deposit with respect to the nominal vertex and E_γ is the energy deposit measured in the LUMI photon calorimeter.

The full event information was available at the third-level trigger (TLT). Tighter timing cuts as well as algorithms to remove beam-halo muons and cosmic rays were applied. The quantity δ_{TLT} was determined using the reconstructed vertex and the events were required to have $\delta_{TLT} > (30\ \text{GeV} - 2E_\gamma)$. Finally, events were accepted if a scattered positron candidate with energy greater than 4 GeV was found. To ensure full containment of the shower in the calorimeter, events in which the scattered positron was located within 2 cm of the beamhole were rejected.

In total 1,747,944 (3,935,516) NC DIS candidates satisfied the above low-Q^2 (high-Q^2) trigger condition.

5 Reconstruction of event kinematics

In the determination of the event kinematics, the CAL energy deposits were separated into two categories: those associated with the identified scattered positron, and all other energy deposits. The latter were defined as the hadronic energy. The kinematics of the event was then determined from:

- the energy (E'_e) and polar angle (θ_e) of the scattered positron;
- the hadronic energy expressed in terms of the longitudinal:

$$\delta_h = \sum_h (E_h - P_{Z,h})$$

and transverse:

$$P_{T,h} = \sqrt{(\sum_h P_{X,h})^2 + (\sum_h P_{Y,h})^2}$$

components, where the sums run over all energy deposits not associated with the scattered positron.

The hadronic energy flow is characterised by an angle γ_h defined by

$$\cos\gamma_h = \frac{P_{T,h}^2 - \delta_h^2}{P_{T,h}^2 + \delta_h^2}. \tag{4}$$

In the quark-parton model, the angle γ_h corresponds to the polar angle of the struck quark.

The following refinements in the calculation of γ_h were applied in order to optimise the accuracy and precision of the reconstruction:

- the transverse momentum of the hadronic system, $P_{T,h}$, was replaced by the more accurately measured transverse momentum of the scattered positron, $P_{T,e}$;
- at low values of δ_h, part of the hadronic system escapes detection through the forward beamhole. A parameterisation, determined from MC simulation, as a function of the measured ratio $P_{T,h}/P_{T,e}$, γ_h and Q^2 was used to correct δ_h:

$$\delta_{h,\text{cor}} = \delta_h\, \mathcal{C}(P_{T,h}/P_{T,e}, \gamma_h, Q^2); \tag{5}$$

- in the determination of y at large values of δ_h, the information from the positron provides the most accurate measurement, $y_e = 1 - (E'_e/2E_e)(1 - \cos\theta_e)$. However, at low values of δ_h, the hadronic information provides a more accurate measurement, $y_{\text{cor}} = \delta_{h,\text{cor}}/(2E_e)$. The Σ-correction [13] combines y_{cor} and y_e such that

$$y_{\Sigma,\text{cor}} = \frac{\delta_{h,\text{cor}} y_e + \delta_e y_{\text{cor}}}{\delta_e + \delta_{h,\text{cor}}},$$

where $\delta_e = E'_e(1 - \cos\theta_e)$;
- finally, γ_{PT} was calculated from:

$$\cos\gamma_{\text{PT}} = \frac{P_{T,e}^2 - \delta_{\Sigma,\text{cor}}^2}{P_{T,e}^2 + \delta_{\Sigma,\text{cor}}^2}, \tag{6}$$

where $\delta_{\Sigma,\text{cor}} = 2E_e\, y_{\Sigma,\text{cor}}$.

For the present analysis, the PT method [1] was used to reconstruct the kinematic variables of the events:

$$Q^2_{\text{PT}} = 4E_e^2 \frac{\sin\gamma_{\text{PT}}(1 + \cos\theta_e)}{\sin\gamma_{\text{PT}} + \sin\theta_e - \sin(\gamma_{\text{PT}} + \theta_e)};$$

$$x_{\text{PT}} = \frac{E_e}{E_p} \frac{\sin\gamma_{\text{PT}} + \sin\theta_e + \sin(\gamma_{\text{PT}} + \theta_e)}{\sin\gamma_{\text{PT}} + \sin\theta_e - \sin(\gamma_{\text{PT}} + \theta_e)};$$

$$y_{\text{PT}} = \frac{Q^2_{\text{PT}}}{s x_{\text{PT}}};$$

$$W^2_{\text{PT}} = Q^2_{\text{PT}} \frac{1 - x_{\text{PT}}}{x_{\text{PT}}} + m_p^2.$$

This reconstruction method achieves good resolution and minimises biases in x and Q^2 over the full kinematic range.

6 Monte Carlo simulation

Monte Carlo (MC) event simulation was used to correct for detector acceptance and resolution effects. The detector simulation is based on the GEANT program [14] and incorporates the best understanding of the detector and the trigger, including test-beam results. Neutral current DIS events were simulated with radiative effects using the HERACLES 4.5.2 [15] program interfaced to the LEPTO 6.5 [16] MC program by the DJANGO6 2.4 program [17]. HERACLES includes $O(\alpha)$ leptonic corrections for initial- and final-state radiation, and one-loop vertex and propagator corrections. In addition, leading logarithmic effects to order $O(\alpha\alpha_s)$ are included. The hadronic final state was simulated using the colour-dipole model CDMBGF [18] including all leading-order QCD diagrams as implemented in ARIADNE 4.08 [20] for the QCD cascade and JETSET 7.4 [21] for the hadronisation. The ARIADNE model provides the best description of the characteristics of the DIS non-diffractive hadronic final state [22]. Diffractive events which are characterised by a large rapidity gap in the detector [23,24] were simulated within ARIADNE, which was interfaced to the RAPGAP 2.06/52 [25] program. The latter assumes that the struck quark belongs to a colourless state having only a small fraction of the proton momentum. The diffractive and non-diffractive samples were mixed as a function of $x_{\rm PT}$ and $Q^2_{\rm PT}$ as determined from the η_{max} distribution in the data, where η_{max} is the pseudorapidity of the most forward energy deposit with more than 400 MeV. The overall normalisation was kept fixed. The CTEQ4D [26] parton density parameterisations were used in the simulations.

The vertex distribution used in the simulation was taken from DIS events having both scattered positrons and hadrons well reconstructed by the CTD. The vertex finding efficiency is well described by the MC simulation, as is shown below (see Sect. 7.1).

The effects of the uranium radioactivity were studied in randomly triggered events. The energy deposits in these events originate entirely from the calorimeter noise. The rate and energy distribution were simulated in the MC program.

Twelve different MC samples with varying Q^2 ranges were generated with integrated luminosities increasing with Q^2, from 1.2 pb^{-1} for $Q^2 > 0.5$ GeV^2 to 1500 fb^{-1} for $Q^2 > 40000$ GeV^2. The fluctuations in the final result due to the MC-sample statistics are small.

The main source of background in the data comes from photoproduction interactions that led to the detection of a fake scattered positron. Resolved and direct photoproduction events [27] were simulated using PYTHIA 5.724 [21], with the total cross section given by the ALLM parameterisation [28]. Resolved and direct photoproduction events, corresponding to integrated luminosities of 0.7 and 2.5 pb^{-1}, respectively, were generated with $y > 0.36$. Events with smaller y values do not contribute to the photoproduction background due to the requirement on δ.

7 Positron identification and measurement

The positron-identification algorithm is based on a neural network using information from the CAL [29]. The network separates energy deposits in the calorimeter that are due to electromagnetic showers from those that are of hadronic origin by assigning a 'positron-probability' value. If more than one positron is identified, the one with the highest probability is taken to be the scattered positron. Monte Carlo studies show that the efficiency for finding the scattered positron increases from 70% at 8 GeV to greater than 99% for energies above 25 GeV. This was checked by using QED-Compton events. The results obtained from the neural network were compared to an alternative positron-finding algorithm [30]. Systematic differences of the order of 2% were observed at 8 GeV, decreasing to less than 1% for energies higher than 15 GeV.

7.1 Positron angle measurement

The scattering angle of the positron was determined using either its impact position on the CAL inner face and the event vertex or from a reconstructed track in the CTD. For $\theta_e \lesssim 150^\circ$, the scattered positron registers in the three innermost superlayers of the CTD and the parameters of the reconstructed track, matched to the positron impact position, were used.

For $\theta_e \gtrsim 150^\circ$, the impact position of the scattered positron on the inner face of the calorimeter was reconstructed using other detector elements. The SRTD information was used, when available; otherwise the HES information was used. If neither HES nor SRTD information was available, then the CAL reconstruction was used:

- SRTD – the positron position in the SRTD was determined from the centres of gravity of the pulse-heights of the strips in the X and Y planes of the SRTD. The measured position resolution was 3 mm. For a subset of these positrons, the position measured by the SRTD was compared to the result from the track measurement. The resolution of the RTD-SRTD matching was 3 mm and systematic deviations were less than 1 mm;
- HES – the position in the HES was determined from the pulse-height sharing in the pads. The position measurement was checked by matching tracks and positron candidates. The resolution of the track-HES matching was 5 mm with systematic deviations smaller than 1.5 mm;
- CAL – the position of a shower in the CAL was determined using the relative pulse-height of the left and right PMTs and energy deposits in neighbouring cells. The position resolution on the face of the CAL was about 10 mm. The alignment of the calorimeter was checked by matching tracks and positron candidates in the CAL. The resolution of the track-CAL matching was 10 mm with systematic biases of less than 2 mm.

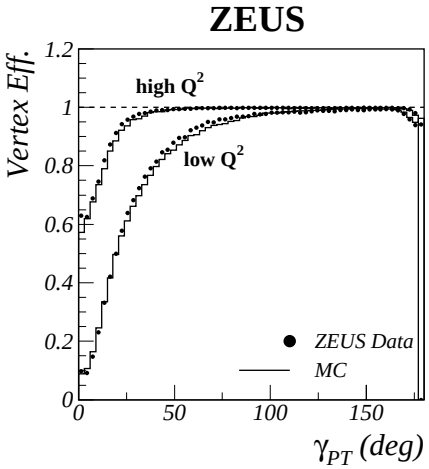

Fig. 2. Vertex finding efficiency as a function of the hadronic angle $\gamma_{\rm PT}$, defined in (6)

The coordinates of the event vertex were determined from tracks reconstructed with the CTD. The Z coordinate ($Z_{\rm vertex}$) was determined on an event-by-event basis. However, since the transverse sizes of the beams were smaller than the resolutions for the X and Y coordinates, the average X and Y vertex positions per beam fill were used. For events not having a tracking vertex, the Z coordinate was set to $Z = 0$, the nominal position of the interaction point averaged over all runs.

The probability of finding a vertex depended on the number of particles detected in the tracking detectors and thus mainly on the hadronic angle, γ_h. Figure 2 shows the fraction of events having a reconstructed vertex as a function of $\gamma_{\rm PT}$. For $\gamma_{\rm PT} > 70°$, the vertex efficiency was greater than 95%. In the low-Q^2 sample, it decreased to about 50% for events with $\gamma_{\rm PT} \sim 20°$. The MC simulation reproduces the observed behaviour well. The drop in vertex-finding efficiency near $\gamma_{\rm PT} = 174°$ results from the combination of the characteristics of the DIS final states and the acceptance of the CTD in the rear direction. At low $\gamma_{\rm PT}$, the vertex-finding efficiency is higher for high-Q^2 events, since the scattered positron is detected more often by the CTD.

The Z coordinate of the vertex can also be determined from the measurements of the arrival times of energy deposits in the FCAL. The corresponding resolution is $\sigma_Z^{\rm timing} = 9$ cm. This determination was only used for studies of systematic uncertainties.

For polar angles $17.2° \lesssim \theta_e \lesssim 150°$ and positron momenta > 5 GeV, the tracking efficiency was greater than 98%. Thus, when the impact position on the CAL inner face was outside a radius of 80 cm around the beampipe, corresponding to a scattering angle of 150° for events with $Z = 0$, a track was required to match the positron identified in the CAL and the polar angle was taken from the track parameters. A successful match required that the distance between the extrapolated impact point of the track on the face of the CAL and the position determined by the CAL was less than 10 cm.

The resolution of the scattering-angle measurement was $\sigma_{\theta_e}^{\rm SRTD} \backsimeq 2.0$ mrad for positrons reconstructed in the SRTD, $\sigma_{\theta_e}^{\rm HES} \backsimeq 3.4$ mrad for positrons measured in the HES, $\sigma_{\theta_e}^{\rm CAL} \backsimeq 6.8$ mrad for positrons measured in the CAL and $\sigma_{\theta_e}^{\rm track} \backsimeq 2.6$ mrad for positrons with a matched track.

7.2 Positron energy determination

The scattered positron loses energy in the passive material in front of the CAL. In the region used for this analysis, this corresponds to about 1.2 radiation lengths except in areas around the rear beampipe, $\theta \gtrsim 170°$, and the solenoid support structure, $130° \lesssim \theta \lesssim 145°$, where it corresponds to 2.0 and 2.5 radiation lengths, respectively. In the analysis, the CAL measurement of the scattered positron energy was corrected for these energy losses.

The correction was determined directly from the data using the following subsamples:

- at low y, the scattered-positron energy is kinematically constrained to be close to the positron beam energy and to be primarily a function of the scattering angle. For these events, called kinematic-peak (KP) events, the mean positron energy can be determined from the scattering angle ($E'_e \approx 2E_e/(1-\cos\theta_e)$) to within 0.5%. The KP events were selected by requiring $y_{JB} = \delta_h/(2E_e) < 0.04$ [31], and provide an energy calibration at $E'_e \approx E_e = 27.5$ GeV for $\theta \gtrsim 135°$;
- the double-angle (DA) method [32] predicts the positron energy from the angular information of the scattered positron and the hadrons, $E'_e = (2E_e \sin\gamma_h)/(\sin\gamma_h + \sin\theta_e - \sin(\gamma_h+\theta_e))$. This relation was used to relate the energy loss in passive material to the SRTD and PRES signal, in the energy range $15 \lesssim E'_e \lesssim 25$ GeV, assuming no hard QED radiation in the initial state;
- for QED-Compton events ($ep \to e\gamma p$) observed in the main detector, the energies of the positron and the photon can be predicted precisely from the measurement of their scattering angles since the transverse momentum of the scattered proton is small. QED-Compton events provide a calibration for $5 \lesssim E'_e \lesssim 20$ GeV and $\theta \gtrsim 160°$;
- in the range $17.2° \lesssim \theta \lesssim 150°$, the momenta of the positrons can be independently determined from the CTD.

For scattered positrons in the RCAL, the correlation between the energy lost in the passive material in front of the calorimeter and the energy deposited in the SRTD or presampler was used to correct the calorimeter energy measurement. The corrections were determined using the KP and DA samples. The QED-Compton events were used as a check on the correction.

The uncertainty in the energy determination, after all corrections, was 2% at 8 GeV, falling linearly to 1% at 15 GeV. In the region covered by BCAL and FCAL, $\theta \lesssim 130°$, the positron cluster energy was corrected based on

material maps implemented in the detector simulation package. For scattered positrons in the BCAL [30] and RCAL, the corrections for non-uniformities due to geometric effects caused by cell and module boundaries were also made. Identical studies were also performed on the event samples generated by the MC simulations. The resulting corrections were applied to the events generated in the MC simulation.

8 Hadronic energy determination

Energy deposits coming from the hadronic final state were used to evaluate the quantities δ_h and $P_{T,h}$. These energy deposits, unlike those of the positron, were not corrected for energy loss in the passive material. Instead, a combination of clusters of energy deposits in the CAL and the corresponding tracks measured in the CTD were used in determining the hadronic energy [33]. The selected calorimeter clusters and tracks are referred to as energy-flow objects (EFOs). The use of track information reduces the sensitivity to energy losses in inactive material in front of the CAL. However, the energies of particles for which no track information was available (e.g., because the energy was deposited by a neutral particle) were measured using the CAL alone.

Monte Carlo studies of the calorimeter response indicated that the uncorrected γ_h calculated with (4) was biased by hadronic energy coming from interactions in material between the primary vertex and the calorimeter or by backsplash from the calorimeter (albedo), primarily from the FCAL. To minimise this bias, neutral clusters with energy below 3 GeV and with polar angles larger than a $\gamma_{\max}$, $\gamma_{\max} = \gamma_h + 50^\circ$, were removed on an event-by-event basis. The choice of 50° was derived from the MC simulation by minimising the dependence of δ_h on $\gamma_{\max}$. For the values of $\gamma_{\max}$ used, the biases in δ_h and $P_{T,h}$ were small. The agreement between data and MC simulation of the distributions of removed energies for different γ_h ranges was also good. After a first pass of cluster removal, the value of γ_h was re-calculated and the procedure repeated until it converged, typically after two or three iterations. Removing calorimeter clusters in this manner substantially improved the resolution and reduced the bias of the quantities δ_h and $P_{T,h}$ at low values of δ_h (corresponding to small values of y) and left them largely unchanged for large values of δ_h.

The transverse momentum of the positron, $P_{T,e}$, calculated using the positron energy, corrected as described in the previous section, was compared to the $P_{T,h}$ of the hadrons in both the MC simulation and the data. Uncertainties in the determination of the hadronic energy were estimated from this comparison. The Monte Carlo simulation of the mean $P_{T,h}/P_{T,e}$ as a function of γ_h agrees within 2% with the data for the entire kinematic range covered in this paper. Based on these comparisons, an uncertainty of $\pm 2\%$ was assigned to the hadronic-energy measurement, neglecting the uncertainty due to the angular information in the calculation of $P_{T,h}$, which is small.

9 Data sample

9.1 Event selection

The following cuts, using the energy and angle of the scattered positron, were used both to select NC DIS events and to reject background:

- a positron candidate, defined as described in Sect. 7;
- $E'_e > 8$ GeV, where E'_e is the corrected positron energy. This cut ensured high and well understood positron finding efficiency and suppressed background from photoproduction;
- events with an impact point of the scattered positron on the RCAL inside a box of $26 \times 14\,\mathrm{cm}^2$ centred around the beampipe were rejected ("box cut"). This ensured that the impact point was at least 2.5 cm away from the edge of the RCAL and therefore guaranteed full containment of the electromagnetic shower in the calorimeter. Events in which the scattered positron traversed the rear cooling pipes around the beampipe were also rejected. In the high-Q^2 sample, events with an impact point of the scattered positron on the RCAL inside a radius of 28 cm around the beampipe were also rejected;
- a track match for $17.2^o < \theta_e \lesssim 150^\circ$. This condition suppressed events from cosmic rays, halo-muons, photoproduction and DIS events in which an electromagnetic shower was falsely identified as the scattered positron;
- to reduce photoproduction background further, isolated positrons were selected by requiring no more than a total of 5 GeV from all calorimeter cells not associated with the scattered positron in an $\eta - \phi$ cone of radius 0.8 centred on the positron.

The hadronic information was used in the following selection criteria:

- $38 < \delta < 65$ GeV, where $\delta = \sum_i (E_i - P_{Zi})$. Here the sum runs over both the energy-flow objects from the hadronic system and the energy deposits belonging to the identified positron. This cut removed events with large initial-state radiation and further reduced the background from photoproduction. For events with a scattered positron beyond the tracking acceptance ($\theta_e < 17.2^o$), the minimum requirement was raised to $\delta > 44$ GeV;
- $P_{T,h}/P_{T,e} > 0.3$. For the PT method to yield a reliable measurement of x and Q^2, the loss of hadronic transverse momentum must be small. In some events, a substantial part of the current jet remained in the forward beampipe. These events, produced at small γ_h, could be falsely reconstructed at large γ_h due to the CAL noise or backsplash. This cut suppressed such events.

Finally, the following cuts were applied:

- $y_e < 0.95$. This condition removes events where fake positrons are found in the FCAL;
- -50 cm $< Z_{\mathrm{vertex}} < 50$ cm. This cut was applied to events with a reconstructed tracking vertex; it suppressed beam-gas background events and the small

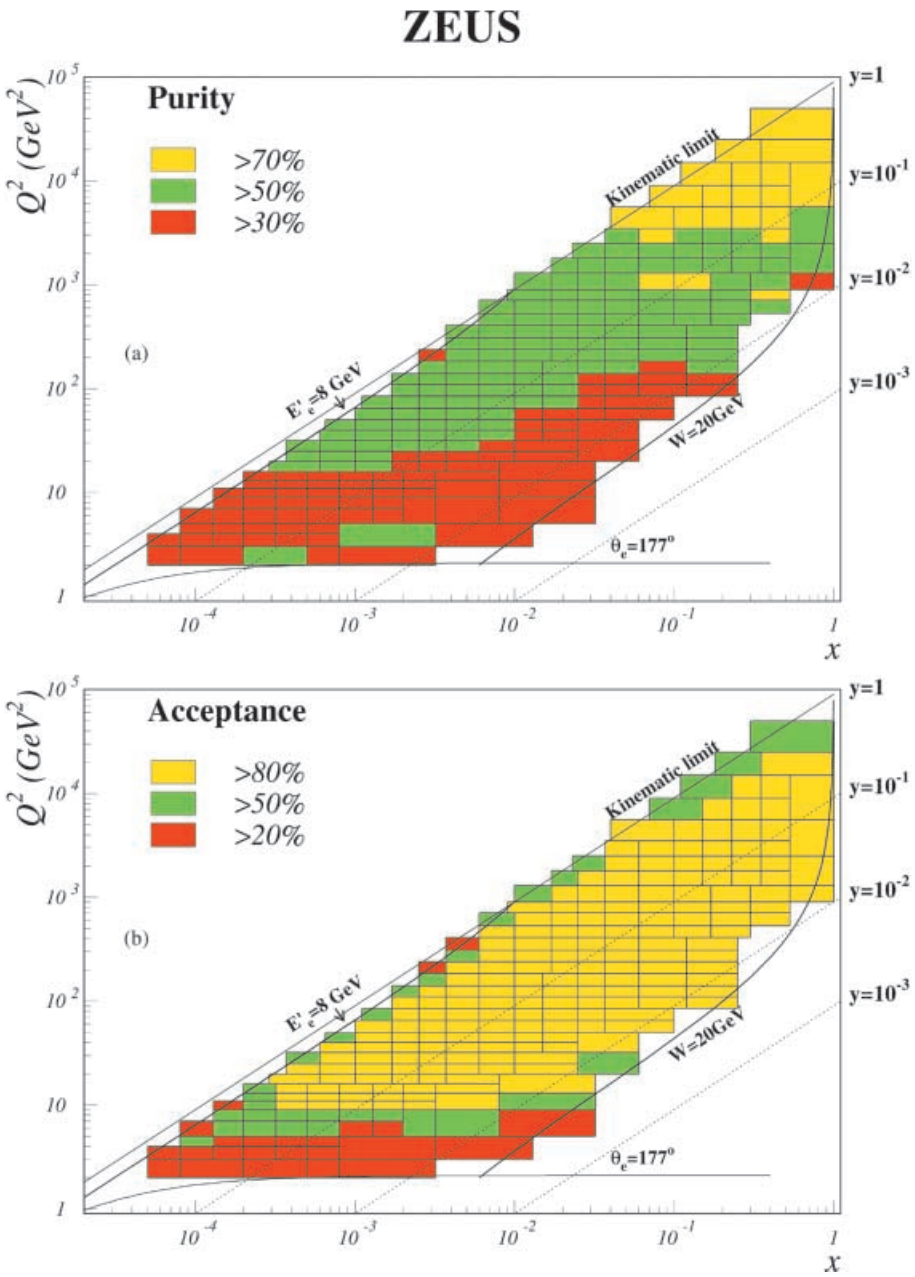

Fig. 3. **a** The purity. **b** The acceptance. The analysis binning is shown, together with the limits of the ZEUS acceptance. At the edges of the kinematic plane, the acceptance is lower due to the various selection criteria. The rear beamhole limits the acceptance of events with small angles of the scattered positron to $Q^2 \gtrsim 2$ GeV^2. For $y \gtrsim 0.7$, the positron-energy cut and for $Q^2 \gtrsim 1000$ GeV^2 and $y = 1$ the kinematic limit of HERA constrains the measurements. The forward beamhole limits the acceptance to $y \gtrsim 0.004$ for events with small angles of the hadronic system; this limit is shown by the line $W = 20$ GeV

fraction of the events in which the vertex position was incorrectly measured. Events without a tracking vertex were accepted and were assigned the mean vertex Z position;

– $W_{\rm PT} > 20$ GeV. This cut, corresponding to $y \gtrsim 0.004$ for $Q^2 \lesssim 400$ GeV^2, selected the kinematic region where a reliable measurement could be made. Events below this cut failed the acceptance and purity requirements described in Sect. 9.2. At low W, the hadronic system is partially lost in the forward beampipe and therefore the measurements are sensitive to the detailed simulation of the beampipe region.

A total of 561,405 (1,300,887) events passed the low (high) Q^2 selection cuts.

9.2 Binning and resolution

The relative resolution in x improves from approximately 35% at $y \sim 0.005$, to ∼11% for $y > 0.1$. The relative resolution in Q^2 is ∼2% for $y \sim 0.1$ and deteriorates to approximately 5% at $y \gtrsim 0.5$ and ∼10% at $y \lesssim 0.01$. For $Q^2 > 400$ GeV^2, the Q^2 relative resolution is approximately 2.5%.

The (x,Q^2)-bins used for the determination of the structure function are shown in Fig. 3. The numbers of events in each of the bins are given in Table 1. The bins were chosen commensurate with the resolutions. At large Q^2 and also at low y, larger bin sizes were chosen to obtain adequate statistics in each bin and to minimise bin-to-bin migrations as a result of the non-Gaussian tails. Further-

Table 1. Results for the reduced cross section and the structure function F_2^{em}. The relative corrections in the last three columns are defined in Sect. 10.1

Q^2 (GeV^2)	x	y	N_{data}	N_{php}	$\tilde{\sigma}^{e^+p}$	δ_{stat} (%)	δ_{sys} (%)	F_2^{em}	Δ_{all} (%)	Δ_{F_2} (%)	Δ_{xF_3} (%)	Δ_{F_L} (%)
2.7	$6.32{\cdot}10^{-5}$	0.474	9506	769	0.832	1.7	4.7	0.869	-4.3	0.0	0.0	-4.3
2.7	$1.61{\cdot}10^{-4}$	0.186	21489	229	0.740	1.0	2.4	0.744	-0.6	0.0	0.0	-0.6
2.7	$4.00{\cdot}10^{-4}$	0.075	18716	47	0.649	1.1	3.9	0.650	-0.1	0.0	0.0	-0.1
2.7	$6.32{\cdot}10^{-4}$	0.047	8745	13	0.607	1.5	4.3	0.607	0.0	0.0	0.0	0.0
2.7	$2.00{\cdot}10^{-3}$	0.015	23981	6	0.477	0.9	4.2	0.477	0.0	0.0	0.0	0.0
3.5	$6.32{\cdot}10^{-5}$	0.614	5960	1422	1.076	2.7	12.7	1.177	-8.6	0.0	0.0	-8.6
3.5	$1.02{\cdot}10^{-4}$	0.380	6859	354	0.951	2.0	3.6	0.979	-2.9	0.0	0.0	-2.9
3.5	$1.61{\cdot}10^{-4}$	0.241	5818	62	0.882	2.0	2.5	0.891	-1.0	0.0	0.0	-1.0
3.5	$2.53{\cdot}10^{-4}$	0.153	6258	32	0.829	1.9	2.4	0.833	-0.4	0.0	0.0	-0.4
3.5	$4.00{\cdot}10^{-4}$	0.097	5676	0	0.787	1.9	2.7	0.788	-0.1	0.0	0.0	-0.2
3.5	$6.32{\cdot}10^{-4}$	0.061	5619	3	0.700	1.9	3.0	0.701	-0.1	0.0	0.0	-0.1
3.5	$2.00{\cdot}10^{-3}$	0.019	25800	11	0.554	0.9	2.5	0.554	0.0	0.0	0.0	0.0
3.5	$8.00{\cdot}10^{-3}$	0.005	17413	0	0.472	1.0	6.3	0.472	0.0	0.0	0.0	0.0
4.5	$1.02{\cdot}10^{-4}$	0.489	6886	824	1.125	2.0	5.8	1.189	-5.4	0.0	0.0	-5.4
4.5	$1.61{\cdot}10^{-4}$	0.310	5020	107	0.994	2.0	2.2	1.013	-1.9	0.0	0.0	-1.9
4.5	$2.53{\cdot}10^{-4}$	0.197	4476	10	0.923	2.0	2.6	0.929	-0.7	0.0	0.0	-0.7
4.5	$4.00{\cdot}10^{-4}$	0.125	3877	1	0.882	2.2	2.4	0.884	-0.3	0.0	0.0	-0.3
4.5	$6.32{\cdot}10^{-4}$	0.079	3708	5	0.803	2.2	2.0	0.804	-0.1	0.0	0.0	-0.1
6.5	$1.02{\cdot}10^{-4}$	0.706	6501	1382	1.210	2.4	10.2	1.392	-13.1	0.0	0.0	-13.1
6.5	$1.61{\cdot}10^{-4}$	0.448	9445	732	1.159	1.5	3.6	1.213	-4.4	0.0	0.0	-4.4
6.5	$2.53{\cdot}10^{-4}$	0.285	9279	159	1.078	1.5	1.9	1.094	-1.5	0.1	0.0	-1.6
6.5	$4.00{\cdot}10^{-4}$	0.180	7217	33	0.972	1.5	1.8	0.977	-0.6	0.0	0.0	-0.6
6.5	$6.32{\cdot}10^{-4}$	0.114	6435	7	0.898	1.6	3.1	0.900	-0.2	0.0	0.0	-0.2
6.5	$1.02{\cdot}10^{-3}$	0.071	6100	7	0.828	1.6	2.1	0.828	-0.1	0.0	0.0	-0.1
6.5	$1.61{\cdot}10^{-3}$	0.045	4958	11	0.740	1.8	2.5	0.740	0.0	0.0	0.0	0.0
6.5	$2.53{\cdot}10^{-3}$	0.028	9848	1	0.666	1.2	1.9	0.666	0.0	0.0	0.0	0.0
6.5	$5.00{\cdot}10^{-3}$	0.014	17517	0	0.576	0.9	4.1	0.576	0.0	0.0	0.0	0.0
6.5	$2.10{\cdot}10^{-2}$	0.003	11829	0	0.487	1.2	8.7	0.487	0.0	0.0	0.0	0.0
8.5	$1.61{\cdot}10^{-4}$	0.585	5783	1219	1.212	2.5	9.9	1.323	-8.4	0.0	0.0	-8.3
8.5	$2.53{\cdot}10^{-4}$	0.372	7175	321	1.188	1.6	2.7	1.223	-2.8	0.0	0.0	-2.9
8.5	$4.00{\cdot}10^{-4}$	0.236	6460	111	1.067	1.6	2.0	1.078	-1.0	0.0	0.0	-1.0
8.5	$6.32{\cdot}10^{-4}$	0.149	6028	24	0.973	1.6	2.8	0.977	-0.4	0.0	0.0	-0.4
8.5	$1.02{\cdot}10^{-3}$	0.092	5597	16	0.875	1.6	1.6	0.877	-0.1	0.0	0.0	-0.1
8.5	$1.61{\cdot}10^{-3}$	0.059	4719	8	0.813	1.8	1.6	0.813	0.0	0.0	0.0	-0.1
10	$1.61{\cdot}10^{-4}$	0.689	2222	570	1.230	4.2	12.8	1.400	-12.1	0.1	0.0	-12.2
10	$2.53{\cdot}10^{-4}$	0.438	4923	485	1.237	2.1	4.5	1.291	-4.2	0.0	0.0	-4.1
10	$4.00{\cdot}10^{-4}$	0.277	4588	125	1.099	1.9	2.3	1.115	-1.4	0.0	0.0	-1.4
10	$6.32{\cdot}10^{-4}$	0.175	4665	23	1.016	1.8	1.9	1.021	-0.5	0.0	0.0	-0.5
10	$1.02{\cdot}10^{-3}$	0.109	4575	1	0.934	1.8	1.9	0.935	-0.2	0.0	0.0	-0.2
10	$1.61{\cdot}10^{-3}$	0.069	3729	4	0.851	2.1	2.0	0.852	-0.1	0.0	0.0	-0.1
10	$2.53{\cdot}10^{-3}$	0.044	3879	5	0.761	2.0	2.4	0.761	0.0	0.0	0.0	0.0
10	$5.00{\cdot}10^{-3}$	0.022	11983	4	0.624	1.1	2.9	0.624	0.0	0.0	0.0	0.0
10	$2.10{\cdot}10^{-2}$	0.005	12719	0	0.503	1.1	6.8	0.503	0.0	0.0	0.0	0.0
12	$2.53{\cdot}10^{-4}$	0.526	3380	557	1.322	2.6	7.5	1.410	-6.3	0.0	0.0	-6.2
12	$4.00{\cdot}10^{-4}$	0.333	3427	169	1.191	2.3	2.7	1.217	-2.2	0.0	0.0	-2.1
12	$6.32{\cdot}10^{-4}$	0.211	3485	32	1.070	2.1	2.3	1.078	-0.7	0.0	0.0	-0.8
12	$1.02{\cdot}10^{-3}$	0.130	3402	4	0.983	2.0	1.9	0.985	-0.3	0.0	0.0	-0.3
12	$1.61{\cdot}10^{-3}$	0.083	2929	6	0.899	2.2	1.6	0.900	-0.1	0.0	0.0	-0.1
12	$2.53{\cdot}10^{-3}$	0.053	2915	1	0.793	2.1	1.9	0.794	0.0	0.0	0.0	0.0
15	$2.53{\cdot}10^{-4}$	0.657	2479	400	1.397	2.9	7.6	1.559	-10.4	0.1	0.0	-10.5
15	$4.00{\cdot}10^{-4}$	0.416	3486	255	1.258	2.3	3.7	1.303	-3.5	0.0	0.0	-3.5
15	$6.32{\cdot}10^{-4}$	0.263	3736	79	1.137	2.0	2.2	1.151	-1.2	0.0	0.0	-1.2
15	$1.02{\cdot}10^{-3}$	0.163	3779	15	1.055	1.9	1.9	1.059	-0.4	0.0	0.0	-0.4
15	$1.61{\cdot}10^{-3}$	0.103	3126	4	0.944	2.2	1.6	0.945	-0.1	0.0	0.0	-0.2

Table 1. (continued)

Q^2 (GeV^2)	x	y	N_{data}	N_{php}	$\tilde{\sigma}^{e^+p}$	δ_{stat} (%)	δ_{sys} (%)	F_2^{em}	Δ_{all} (%)	Δ_{F_2} (%)	Δ_{xF_3} (%)	Δ_{F_L} (%)
15	$2.53{\cdot}10^{-3}$	0.066	3182	0	0.836	2.1	1.6	0.837	0.0	0.0	0.0	-0.1
15	$5.00{\cdot}10^{-3}$	0.033	5672	3	0.706	1.5	1.5	0.706	0.0	0.0	0.0	0.0
15	$2.10{\cdot}10^{-2}$	0.008	13289	0	0.519	1.0	6.9	0.519	0.0	0.0	0.0	0.0
18	$5.00{\cdot}10^{-4}$	0.399	4653	424	1.284	1.9	4.1	1.325	-3.1	0.0	0.0	-3.1
18	$8.00{\cdot}10^{-4}$	0.249	3646	53	1.157	2.2	2.4	1.169	-1.0	0.0	0.0	-1.0
18	$1.30{\cdot}10^{-3}$	0.154	3571	8	1.038	2.0	2.2	1.041	-0.3	0.0	0.0	-0.3
18	$2.10{\cdot}10^{-3}$	0.095	2475	3	0.929	2.3	1.6	0.930	-0.1	0.0	0.0	-0.1
18	$3.20{\cdot}10^{-3}$	0.062	2421	5	0.851	2.4	1.8	0.851	0.0	0.0	0.0	0.0
18	$5.00{\cdot}10^{-3}$	0.040	4363	1	0.739	1.7	1.7	0.739	0.0	0.0	0.0	0.0
22	$5.00{\cdot}10^{-4}$	0.488	2430	184	1.357	2.5	4.0	1.425	-4.8	0.1	0.0	-4.8
22	$8.00{\cdot}10^{-4}$	0.305	2884	51	1.267	2.2	1.9	1.287	-1.6	0.0	0.0	-1.6
22	$1.30{\cdot}10^{-3}$	0.188	2830	15	1.065	2.3	2.3	1.071	-0.6	0.0	0.0	-0.5
22	$2.10{\cdot}10^{-3}$	0.116	2033	2	1.001	2.7	2.0	1.003	-0.2	0.0	0.0	-0.2
22	$3.20{\cdot}10^{-3}$	0.076	1986	5	0.905	2.6	1.7	0.905	-0.1	0.0	0.0	-0.1
22	$5.00{\cdot}10^{-3}$	0.049	2268	1	0.771	2.4	1.7	0.771	0.0	0.0	0.0	0.0
22	$8.00{\cdot}10^{-3}$	0.030	2161	0	0.656	2.4	1.7	0.656	0.0	0.0	0.0	0.0
22	$1.30{\cdot}10^{-2}$	0.019	3398	0	0.581	2.0	5.6	0.581	0.0	0.0	0.0	0.0
22	$3.20{\cdot}10^{-2}$	0.008	4541	0	0.512	1.8	6.9	0.512	0.0	0.0	0.0	0.0
27	$5.00{\cdot}10^{-4}$	0.599	1492	99	1.497	3.3	4.0	1.620	-7.6	0.0	0.0	-7.6
27	$8.00{\cdot}10^{-4}$	0.374	2460	58	1.294	2.5	2.2	1.325	-2.4	0.0	0.0	-2.4
27	$1.30{\cdot}10^{-3}$	0.230	2639	16	1.181	2.3	2.7	1.190	-0.8	0.0	0.0	-0.8
27	$2.10{\cdot}10^{-3}$	0.143	1910	4	1.095	2.8	1.7	1.098	-0.3	0.0	0.0	-0.3
27	$3.20{\cdot}10^{-3}$	0.094	1699	2	0.901	2.7	2.1	0.902	-0.1	0.0	0.0	-0.1
27	$5.00{\cdot}10^{-3}$	0.060	2016	0	0.804	2.5	2.5	0.804	0.0	0.0	0.0	0.0
27	$8.00{\cdot}10^{-3}$	0.037	1997	0	0.731	2.6	2.7	0.731	0.0	0.0	0.0	0.0
27	$1.30{\cdot}10^{-2}$	0.023	3210	0	0.634	2.0	2.9	0.634	0.0	0.0	0.0	0.0
35	$8.00{\cdot}10^{-4}$	0.485	23836	950	1.404	1.5	2.9	1.467	-4.3	0.1	0.0	-4.3
35	$1.30{\cdot}10^{-3}$	0.298	25024	204	1.225	1.4	1.8	1.241	-1.3	0.0	0.0	-1.3
35	$2.10{\cdot}10^{-3}$	0.185	17347	15	1.108	1.6	1.6	1.113	-0.5	0.0	0.0	-0.4
35	$3.20{\cdot}10^{-3}$	0.121	16475	5	0.961	1.7	1.6	0.963	-0.2	0.0	0.0	-0.2
35	$5.00{\cdot}10^{-3}$	0.078	19271	13	0.864	1.6	1.5	0.865	0.0	0.0	0.0	-0.1
35	$8.00{\cdot}10^{-3}$	0.049	18246	0	0.727	1.6	1.8	0.727	0.0	0.0	0.0	0.0
35	$1.30{\cdot}10^{-2}$	0.030	13171	0	0.646	1.9	2.2	0.646	0.0	0.0	0.0	0.0
35	$2.10{\cdot}10^{-2}$	0.018	14507	0	0.555	1.8	2.8	0.555	0.0	0.0	0.0	0.0
35	$3.20{\cdot}10^{-2}$	0.012	32311	0	0.496	1.1	7.6	0.496	0.0	0.0	0.0	0.0
45	$8.00{\cdot}10^{-4}$	0.624	13446	697	1.482	1.8	3.6	1.604	-7.6	0.0	0.0	-7.5
45	$1.30{\cdot}10^{-3}$	0.384	20011	245	1.297	1.3	2.1	1.327	-2.2	0.1	0.0	-2.3
45	$2.10{\cdot}10^{-3}$	0.238	14091	56	1.131	1.7	1.7	1.139	-0.7	0.0	0.0	-0.7
45	$3.20{\cdot}10^{-3}$	0.156	13613	5	0.998	1.5	1.5	1.001	-0.3	0.0	0.0	-0.3
45	$5.00{\cdot}10^{-3}$	0.100	15984	2	0.909	1.4	1.3	0.910	-0.1	0.0	0.0	-0.1
45	$8.00{\cdot}10^{-3}$	0.062	15340	0	0.777	1.4	1.5	0.777	0.0	0.0	0.0	0.0
45	$1.30{\cdot}10^{-2}$	0.038	10876	0	0.661	1.7	1.7	0.661	0.0	0.0	0.0	0.0
45	$2.10{\cdot}10^{-2}$	0.024	11920	0	0.587	1.7	2.1	0.587	0.0	0.0	0.0	0.0
60	$1.30{\cdot}10^{-3}$	0.512	18040	373	1.387	1.3	2.2	1.450	-4.3	0.0	0.0	-4.3
60	$2.10{\cdot}10^{-3}$	0.317	13355	143	1.213	1.5	1.8	1.230	-1.3	0.0	0.0	-1.4
60	$3.20{\cdot}10^{-3}$	0.208	13038	31	1.074	1.5	1.5	1.079	-0.5	0.1	0.0	-0.5
60	$5.00{\cdot}10^{-3}$	0.133	15083	6	0.900	1.4	1.5	0.902	-0.2	0.0	0.0	-0.2
60	$8.00{\cdot}10^{-3}$	0.083	14371	0	0.809	1.4	1.5	0.809	0.0	0.0	0.0	-0.1
60	$1.30{\cdot}10^{-2}$	0.051	10381	0	0.689	1.7	1.9	0.689	0.0	0.0	0.0	0.0
60	$2.10{\cdot}10^{-2}$	0.032	11570	0	0.598	1.6	2.4	0.598	0.0	0.1	0.0	0.0
60	$3.20{\cdot}10^{-2}$	0.021	8000	0	0.537	2.0	3.3	0.536	0.0	0.0	0.0	0.0
60	$5.00{\cdot}10^{-2}$	0.013	14942	0	0.512	1.5	6.8	0.512	0.0	0.0	0.0	0.0
70	$1.30{\cdot}10^{-3}$	0.597	9308	144	1.438	1.8	2.2	1.531	-6.1	0.1	0.0	-6.1
70	$2.10{\cdot}10^{-3}$	0.370	10323	142	1.238	1.7	1.9	1.262	-1.9	0.0	0.0	-1.9
70	$3.20{\cdot}10^{-3}$	0.243	9986	17	1.087	1.7	1.6	1.094	-0.6	0.1	0.0	-0.7

Table 1. (continued)

Q^2 (GeV^2)	x	y	N_{data}	N_{php}	$\tilde{\sigma}^{e^+p}$	δ_{stat} (%)	δ_{sys} (%)	F_2^{em}	Δ_{all} (%)	Δ_{F_2} (%)	Δ_{xF_3} (%)	Δ_{F_L} (%)
70	$5.00{\cdot}10^{-3}$	0.155	11939	2	0.984	1.5	1.5	0.986	-0.2	0.0	0.0	-0.2
70	$8.00{\cdot}10^{-3}$	0.097	11402	0	0.815	1.6	1.4	0.815	0.0	0.0	0.0	-0.1
70	$1.30{\cdot}10^{-2}$	0.060	8257	0	0.708	1.9	1.7	0.708	0.0	0.0	0.0	0.0
70	$2.10{\cdot}10^{-2}$	0.037	9567	0	0.620	1.8	1.6	0.620	0.0	0.0	0.0	0.0
70	$3.20{\cdot}10^{-2}$	0.024	6805	0	0.557	2.1	2.8	0.557	0.0	0.0	0.0	0.0
70	$5.00{\cdot}10^{-2}$	0.016	15253	0	0.500	1.6	6.2	0.500	0.0	0.0	0.0	0.0
90	$2.10{\cdot}10^{-3}$	0.475	6476	83	1.236	2.0	2.2	1.277	-3.2	0.1	0.0	-3.3
90	$3.20{\cdot}10^{-3}$	0.312	7362	10	1.168	1.9	1.7	1.182	-1.1	0.0	0.0	-1.2
90	$5.00{\cdot}10^{-3}$	0.200	8940	0	1.029	1.7	1.7	1.032	-0.4	0.1	0.0	-0.4
90	$8.00{\cdot}10^{-3}$	0.125	8642	2	0.896	1.8	1.5	0.897	-0.1	0.1	0.0	-0.1
90	$1.30{\cdot}10^{-2}$	0.077	6311	0	0.749	2.1	1.6	0.749	0.0	0.1	0.0	0.0
90	$2.10{\cdot}10^{-2}$	0.048	7083	0	0.622	1.9	1.9	0.621	0.0	0.1	0.0	0.0
90	$3.20{\cdot}10^{-2}$	0.031	4891	1	0.535	2.3	2.9	0.535	0.0	0.1	0.0	0.0
90	$5.00{\cdot}10^{-2}$	0.020	5982	0	0.484	2.1	6.3	0.484	0.0	0.1	0.0	0.0
90	$8.00{\cdot}10^{-2}$	0.012	7223	0	0.435	2.0	2.8	0.435	0.0	0.0	0.0	0.0
90	$1.80{\cdot}10^{-1}$	0.006	2981	0	0.340	3.1	5.3	0.339	0.1	0.1	0.0	0.0
120	$2.10{\cdot}10^{-3}$	0.634	3273	2	1.317	2.2	2.5	1.404	-6.2	0.1	0.0	-6.2
120	$3.20{\cdot}10^{-3}$	0.416	4812	13	1.173	1.9	2.0	1.198	-2.1	0.1	0.0	-2.2
120	$5.00{\cdot}10^{-3}$	0.266	6066	13	1.038	1.7	1.8	1.045	-0.7	0.1	0.0	-0.7
120	$8.00{\cdot}10^{-3}$	0.166	6203	0	0.908	1.8	1.4	0.910	-0.2	0.1	0.0	-0.2
120	$1.30{\cdot}10^{-2}$	0.102	4477	0	0.760	2.0	1.8	0.760	0.0	0.1	0.0	-0.1
120	$2.10{\cdot}10^{-2}$	0.063	5225	0	0.664	1.9	1.8	0.664	0.0	0.1	0.0	0.0
120	$3.20{\cdot}10^{-2}$	0.042	3712	0	0.579	2.3	2.2	0.579	0.1	0.1	0.0	0.0
120	$5.00{\cdot}10^{-2}$	0.027	4133	0	0.472	2.1	5.1	0.472	0.1	0.1	0.0	0.0
120	$8.00{\cdot}10^{-2}$	0.017	5409	0	0.437	1.9	4.7	0.436	0.0	0.1	0.0	0.0
120	$1.80{\cdot}10^{-1}$	0.007	2653	0	0.328	2.7	8.8	0.328	0.1	0.1	0.0	0.0
150	$3.20{\cdot}10^{-3}$	0.520	3655	7	1.194	2.1	2.3	1.238	-3.6	0.1	-0.1	-3.6
150	$5.00{\cdot}10^{-3}$	0.333	4977	0	1.037	1.9	1.8	1.049	-1.1	0.1	-0.1	-1.2
150	$8.00{\cdot}10^{-3}$	0.208	5111	0	0.887	1.8	1.6	0.890	-0.3	0.1	0.0	-0.4
150	$1.30{\cdot}10^{-2}$	0.128	3912	0	0.805	2.1	2.0	0.805	-0.1	0.1	0.0	-0.1
150	$2.10{\cdot}10^{-2}$	0.079	4382	0	0.661	2.0	1.9	0.660	0.0	0.1	0.0	0.0
150	$3.20{\cdot}10^{-2}$	0.052	3144	0	0.574	2.4	1.7	0.573	0.1	0.1	0.0	0.0
150	$5.00{\cdot}10^{-2}$	0.033	3622	0	0.515	2.2	2.3	0.515	0.1	0.1	0.0	0.0
150	$8.00{\cdot}10^{-2}$	0.021	4716	0	0.431	2.0	5.0	0.431	0.1	0.1	0.0	0.0
150	$1.80{\cdot}10^{-1}$	0.009	2580	0	0.326	2.7	6.4	0.326	0.1	0.1	0.0	0.0
200	$3.20{\cdot}10^{-3}$	0.693	1197	2	1.162	3.8	3.2	1.248	-6.9	0.2	-0.1	-6.9
200	$5.00{\cdot}10^{-3}$	0.443	3151	0	1.065	2.3	2.1	1.087	-2.1	0.2	-0.1	-2.2
200	$8.00{\cdot}10^{-3}$	0.277	3478	0	0.899	2.2	1.8	0.905	-0.6	0.2	-0.1	-0.7
200	$1.30{\cdot}10^{-2}$	0.171	3451	0	0.794	2.2	1.5	0.795	-0.1	0.1	-0.1	-0.2
200	$2.10{\cdot}10^{-2}$	0.106	2248	0	0.659	2.7	1.8	0.659	0.0	0.1	-0.1	-0.1
200	$3.20{\cdot}10^{-2}$	0.069	2142	0	0.570	2.8	1.9	0.570	0.1	0.1	-0.1	0.0
200	$5.00{\cdot}10^{-2}$	0.044	2393	0	0.508	2.8	2.4	0.508	0.1	0.1	0.0	0.0
200	$8.00{\cdot}10^{-2}$	0.028	3124	0	0.434	2.4	2.7	0.433	0.1	0.1	0.0	0.0
200	$1.80{\cdot}10^{-1}$	0.012	2161	0	0.340	2.9	3.7	0.339	0.1	0.1	0.0	0.0
250	$5.00{\cdot}10^{-3}$	0.554	1971	0	1.066	3.0	2.9	1.105	-3.6	0.3	-0.2	-3.7
250	$8.00{\cdot}10^{-3}$	0.346	2446	0	0.927	2.6	1.7	0.937	-1.1	0.2	-0.1	-1.1
250	$1.30{\cdot}10^{-2}$	0.213	2634	0	0.821	2.7	1.8	0.824	-0.3	0.2	-0.1	-0.3
250	$2.10{\cdot}10^{-2}$	0.132	1644	0	0.644	3.5	1.8	0.644	0.0	0.2	-0.1	-0.1
250	$3.20{\cdot}10^{-2}$	0.087	1646	0	0.612	3.4	2.3	0.612	0.1	0.2	-0.1	0.0
250	$5.00{\cdot}10^{-2}$	0.055	1838	0	0.517	3.2	1.8	0.516	0.1	0.2	-0.1	0.0
250	$8.00{\cdot}10^{-2}$	0.035	2365	0	0.445	2.8	5.1	0.445	0.1	0.2	-0.1	0.0
250	$1.80{\cdot}10^{-1}$	0.015	1729	0	0.341	3.2	5.6	0.340	0.1	0.2	0.0	0.0
350	$5.00{\cdot}10^{-3}$	0.776	810	0	1.103	4.4	3.5	1.196	-7.8	0.3	-0.3	-7.8
350	$8.00{\cdot}10^{-3}$	0.485	1924	2	0.988	2.9	2.1	1.011	-2.3	0.3	-0.3	-2.4
350	$1.30{\cdot}10^{-2}$	0.298	2037	0	0.824	2.9	1.7	0.829	-0.6	0.3	-0.2	-0.7

Table 1. (continued)

Q^2 (GeV^2)	x	y	N_{data}	N_{php}	$\tilde{\sigma}^{e^+p}$	δ_{stat} (%)	δ_{sys} (%)	F_2^{em}	Δ_{all} (%)	Δ_{F_2} (%)	Δ_{xF_3} (%)	Δ_{F_L} (%)
350	$2.10{\cdot}10^{-2}$	0.185	1355	0	0.679	3.6	1.9	0.680	-0.1	0.3	-0.2	-0.2
350	$3.20{\cdot}10^{-2}$	0.121	1329	0	0.639	3.6	2.0	0.639	0.0	0.3	-0.2	-0.1
350	$5.00{\cdot}10^{-2}$	0.078	1475	0	0.526	3.4	1.9	0.526	0.1	0.3	-0.1	0.0
350	$8.00{\cdot}10^{-2}$	0.049	1783	0	0.442	3.2	2.6	0.441	0.1	0.3	-0.1	0.0
350	$1.80{\cdot}10^{-1}$	0.022	1465	0	0.328	3.5	1.6	0.328	0.2	0.2	-0.1	0.0
450	$8.00{\cdot}10^{-3}$	0.624	1163	9	0.954	3.5	2.4	0.995	-4.2	0.4	-0.4	-4.2
450	$1.30{\cdot}10^{-2}$	0.384	1331	0	0.854	3.0	1.7	0.864	-1.2	0.4	-0.4	-1.2
450	$2.10{\cdot}10^{-2}$	0.238	932	0	0.702	3.6	1.6	0.704	-0.3	0.4	-0.3	-0.3
450	$3.20{\cdot}10^{-2}$	0.156	854	0	0.579	4.3	1.8	0.579	0.0	0.4	-0.3	-0.1
450	$5.00{\cdot}10^{-2}$	0.100	1009	0	0.511	3.4	1.5	0.511	0.1	0.4	-0.2	0.0
450	$8.00{\cdot}10^{-2}$	0.062	909	0	0.439	3.6	2.3	0.439	0.2	0.4	-0.2	0.0
450	$1.30{\cdot}10^{-1}$	0.038	830	0	0.365	3.8	2.3	0.365	0.2	0.4	-0.2	0.0
450	$2.50{\cdot}10^{-1}$	0.020	588	0	0.264	4.5	7.7	0.263	0.2	0.3	-0.1	0.0
650	$8.00{\cdot}10^{-3}$	0.901	529	0	0.926	4.6	3.2	1.023	-9.4	0.7	-0.8	-9.4
650	$1.30{\cdot}10^{-2}$	0.554	1056	2	0.827	3.3	1.9	0.850	-2.8	0.7	-0.8	-2.7
650	$2.10{\cdot}10^{-2}$	0.343	792	0	0.722	3.8	1.7	0.728	-0.8	0.7	-0.7	-0.8
650	$3.20{\cdot}10^{-2}$	0.225	712	0	0.603	4.0	1.9	0.604	-0.2	0.7	-0.6	-0.3
650	$5.00{\cdot}10^{-2}$	0.144	751	0	0.475	4.3	2.1	0.475	0.1	0.7	-0.5	-0.1
650	$8.00{\cdot}10^{-2}$	0.090	767	0	0.456	3.9	1.5	0.455	0.2	0.6	-0.4	0.0
650	$1.30{\cdot}10^{-1}$	0.055	641	0	0.357	4.2	3.2	0.356	0.3	0.6	-0.3	0.0
650	$2.50{\cdot}10^{-1}$	0.029	495	0	0.250	4.8	3.4	0.249	0.4	0.6	-0.2	0.0
650	$4.00{\cdot}10^{-1}$	0.018	132	0	0.152	9.5	14.5	0.151	0.3	0.4	-0.1	0.0
800	$1.30{\cdot}10^{-2}$	0.682	653	0	0.847	4.5	2.4	0.887	-4.6	0.9	-1.2	-4.3
800	$2.10{\cdot}10^{-2}$	0.422	436	0	0.665	7.5	1.6	0.675	-1.3	0.9	-1.0	-1.2
800	$3.20{\cdot}10^{-2}$	0.277	470	0	0.647	4.9	1.4	0.650	-0.4	0.9	-0.9	-0.4
800	$5.00{\cdot}10^{-2}$	0.177	449	0	0.451	5.0	2.3	0.451	0.0	0.9	-0.8	-0.1
800	$8.00{\cdot}10^{-2}$	0.111	473	0	0.420	5.8	2.6	0.419	0.2	0.8	-0.6	0.0
800	$1.30{\cdot}10^{-1}$	0.068	425	0	0.370	5.2	2.5	0.369	0.3	0.8	-0.5	0.0
800	$2.50{\cdot}10^{-1}$	0.035	337	0	0.260	5.9	1.8	0.259	0.4	0.7	-0.3	0.0
800	$4.00{\cdot}10^{-1}$	0.022	88	0	0.114	11.4	13.5	0.114	0.4	0.7	-0.2	0.0
1200	$1.40{\cdot}10^{-2}$	0.950	376	0	0.872	5.5	2.9	0.960	-9.2	1.6	-2.1	-8.7
1200	$2.10{\cdot}10^{-2}$	0.634	442	0	0.681	5.1	1.8	0.707	-3.7	1.6	-2.3	-3.0
1200	$3.20{\cdot}10^{-2}$	0.416	449	0	0.563	5.0	2.0	0.571	-1.4	1.6	-2.0	-1.0
1200	$5.00{\cdot}10^{-2}$	0.266	525	0	0.490	4.6	1.6	0.493	-0.4	1.5	-1.7	-0.3
1200	$8.00{\cdot}10^{-2}$	0.166	546	0	0.434	5.3	1.5	0.434	0.0	1.5	-1.4	-0.1
1200	$1.30{\cdot}10^{-1}$	0.102	460	0	0.336	5.8	3.1	0.335	0.3	1.4	-1.1	0.0
1200	$2.50{\cdot}10^{-1}$	0.053	392	0	0.254	5.4	2.0	0.253	0.6	1.3	-0.7	0.0
1200	$4.00{\cdot}10^{-1}$	0.033	176	0	0.149	8.1	10.3	0.148	0.7	1.2	-0.5	0.0
1200	$6.50{\cdot}10^{-1}$	0.020	9	0	0.021	35.6	25.1	0.021	0.7	1.0	-0.3	0.0
1500	$2.10{\cdot}10^{-2}$	0.792	206	0	0.666	7.9	6.2	0.710	-6.1	2.2	-3.3	-5.1
1500	$3.20{\cdot}10^{-2}$	0.520	260	0	0.540	10.3	2.0	0.554	-2.5	2.2	-3.1	-1.6
1500	$5.00{\cdot}10^{-2}$	0.333	320	0	0.518	5.8	1.8	0.523	-1.0	2.1	-2.6	-0.5
1500	$8.00{\cdot}10^{-2}$	0.208	338	0	0.476	5.7	2.6	0.477	-0.2	2.0	-2.1	-0.1
1500	$1.30{\cdot}10^{-1}$	0.128	216	0	0.301	11.8	1.9	0.300	0.3	1.9	-1.6	0.0
1500	$1.80{\cdot}10^{-1}$	0.092	202	0	0.313	7.3	5.9	0.311	0.5	1.8	-1.3	0.0
1500	$2.50{\cdot}10^{-1}$	0.067	146	0	0.270	8.6	3.0	0.268	0.7	1.7	-1.0	0.0
1500	$4.00{\cdot}10^{-1}$	0.042	69	0	0.146	12.6	13.7	0.145	0.9	1.6	-0.7	0.0
1500	$6.50{\cdot}10^{-1}$	0.026	11	0	0.012	30.9	19.0	0.012	0.9	1.4	-0.4	0.0
2000	$3.20{\cdot}10^{-2}$	0.693	156	0	0.586	8.3	3.4	0.617	-5.1	3.2	-5.2	-3.1
2000	$5.00{\cdot}10^{-2}$	0.443	195	0	0.476	7.4	2.0	0.487	-2.3	3.2	-4.6	-0.9
2000	$8.00{\cdot}10^{-2}$	0.277	213	0	0.444	7.1	2.0	0.448	-0.9	3.0	-3.7	-0.2
2000	$1.30{\cdot}10^{-1}$	0.171	154	0	0.340	8.3	3.9	0.340	0.0	2.9	-2.8	-0.1
2000	$1.80{\cdot}10^{-1}$	0.123	131	0	0.282	9.1	2.6	0.280	0.4	2.7	-2.3	0.0
2000	$2.50{\cdot}10^{-1}$	0.089	100	0	0.234	10.4	5.3	0.232	0.7	2.5	-1.8	0.0
2000	$4.00{\cdot}10^{-1}$	0.055	58	0	0.170	13.8	10.1	0.169	1.1	2.3	-1.2	0.0

Table 1. (continued)

Q^2 (GeV^2)	x	y	N_{data}	N_{php}	$\tilde{\sigma}^{e^+p}$	δ_{stat} (%)	δ_{sys} (%)	F_2^{em}	Δ_{all} (%)	Δ_{F_2} (%)	Δ_{xF_3} (%)	Δ_{F_L} (%)
3000	$5.00{\cdot}10^{-2}$	0.665	140	0	0.542	8.7	2.1	0.578	-6.2	5.5	-9.4	-2.3
3000	$8.00{\cdot}10^{-2}$	0.416	144	0	0.438	8.5	2.2	0.452	-3.2	5.2	-7.9	-0.6
3000	$1.30{\cdot}10^{-1}$	0.256	110	0	0.325	13.9	4.4	0.329	-1.1	4.9	-5.9	-0.1
3000	$1.80{\cdot}10^{-1}$	0.185	76	0	0.243	11.7	3.8	0.243	-0.2	4.6	-4.8	-0.1
3000	$2.50{\cdot}10^{-1}$	0.133	62	0	0.193	17.7	4.2	0.192	0.6	4.4	-3.7	0.0
3000	$4.00{\cdot}10^{-1}$	0.083	22	0	0.089	21.7	9.1	0.088	1.4	3.9	-2.5	0.0
3000	$6.50{\cdot}10^{-1}$	0.051	9	0	0.016	33.9	15.3	0.016	2.0	3.5	-1.5	0.0
5000	$8.00{\cdot}10^{-2}$	0.693	142	2	0.376	9.0	2.7	0.422	-10.9	9.8	-18.8	-1.9
5000	$1.30{\cdot}10^{-1}$	0.426	76	0	0.284	11.7	2.0	0.302	-6.1	9.2	-14.8	-0.4
5000	$1.80{\cdot}10^{-1}$	0.308	81	0	0.278	11.3	5.2	0.288	-3.3	8.7	-11.9	-0.2
5000	$2.50{\cdot}10^{-1}$	0.222	60	0	0.223	13.2	3.5	0.226	-1.2	8.1	-9.2	-0.1
5000	$4.00{\cdot}10^{-1}$	0.139	31	0	0.126	18.3	5.4	0.125	1.2	7.2	-6.0	0.0
8000	$1.30{\cdot}10^{-1}$	0.682	48	0	0.241	14.5	4.2	0.293	-17.8	15.1	-31.5	-1.3
8000	$1.80{\cdot}10^{-1}$	0.493	43	0	0.272	15.4	5.6	0.311	-12.4	14.2	-26.1	-0.5
8000	$2.50{\cdot}10^{-1}$	0.355	31	0	0.199	18.1	10.8	0.214	-7.2	13.2	-20.2	-0.2
8000	$4.00{\cdot}10^{-1}$	0.222	18	0	0.119	23.8	6.8	0.121	-1.4	11.7	-13.1	0.0
8000	$6.50{\cdot}10^{-1}$	0.136	11	0	0.036	30.6	14.2	0.035	2.8	10.6	-7.9	0.0
12000	$1.80{\cdot}10^{-1}$	0.739	25	0	0.238	20.1	3.7	0.330	-27.9	20.1	-46.7	-1.2
12000	$2.50{\cdot}10^{-1}$	0.532	15	0	0.172	25.9	4.1	0.214	-19.8	18.6	-38.0	-0.4
12000	$4.00{\cdot}10^{-1}$	0.333	7	0	0.084	38.0	3.3	0.092	-8.2	16.6	-24.7	-0.1
20000	$2.50{\cdot}10^{-1}$	0.887	8	0	0.161	35.4	5.2	0.293	-44.9	26.1	-69.5	-1.4
20000	$4.00{\cdot}10^{-1}$	0.554	4	0	0.080	$^{+79}_{-48}$	13.9	0.112	-28.9	23.2	-51.8	-0.3
30000	$4.00{\cdot}10^{-1}$	0.831	1	0	0.039	$^{+230}_{-83}$	6.8	0.086	-53.9	28.2	-81.4	-0.7

more, good acceptance ($A > 20\%$) and purity ($P > 30\%$) were required for each bin. The acceptance was defined as the fraction of events generated in a bin that passed the event selection. The purity was defined as the fraction of events reconstructed in a bin that were generated in that bin. The lowest values of acceptance occur at the lowest Q^2 values where the box cut (see Sect. 9.1) becomes effective. The bins with lowest purity occur at the lowest y values. In the majority of bins, the acceptance is greater than 80% and the purity is greater than 50%, as shown in Fig. 3.

9.3 Background estimate

The final sample contains a small number of background events from the following sources:

- **non-*ep* background.** The background not associated with *ep* collisions was determined from the number of events observed in unpaired or empty bunches. This background was subtracted statistically, taking into account the appropriate ratios of bunch currents and numbers of bunches. It is less than 1% for most bins and reaches 3% for a few bins at low y;
- **photoproduction background.** The events from the photoproduction MC generator PYTHIA were analysed in the same way as the data and the number of events passing the selection cuts in each bin was determined. This number of events was subtracted. In the region $\delta < 40$ GeV, the photoproduction contribution was measured directly through events tagged by the positron tagger, as seen in Fig. 4a. The MC photoproduction background sample was normalised to the measurement at $\delta < 40$ GeV and subtracted bin by bin. The total photoproduction background contribution to each bin is given in Table 1. The maximum background fraction of about 20% occurs in bins at high y and low Q^2.
- **charged current background.** The background from charged current interactions is negligible.

9.4 Event characteristics

Figure 5 shows the characteristics of both low- and high-Q^2 samples of accepted events. To obtain these distributions, the MC events were reweighted to the structure function obtained from the NLO QCD fit to these data (see Sect. 10.4). The energy, angular and transverse momentum distributions are well reproduced by the MC simulation (also indicated in the figures).

Figure 6 shows the distributions in $y_{\rm PT}$, $x_{\rm PT}$ and $Q^2_{\rm PT}$ together with the MC distributions normalised to the integrated luminosity of the data. Good agreement for the high-Q^2 sample is seen.

The discrepancies seen at low y and low Q^2, $Q^2 \lesssim 15$ GeV^2 and $y \lesssim 10^{-2}$, are located in three (x, Q^2)-bins, the highest x bins at $Q^2 = 3.5$, 6.5 and 10 GeV^2, from a total of 242 bins. The systematic uncertainty in this low-y

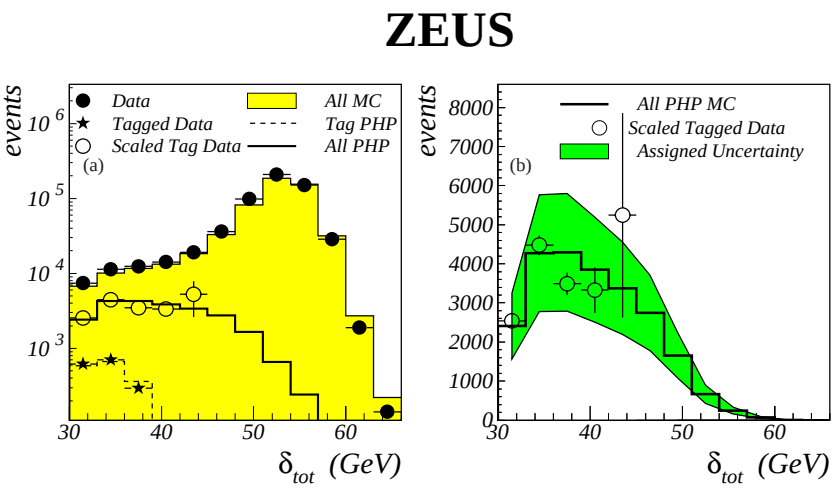

Fig. 4. a Distribution of δ, see (3), for the low-Q^2 sample (filled circles), for that subset of the data tagged by the positron tagger (stars) and for these tagged data corrected for the acceptance of the positron tagger (open circles). The lines show MC distributions after reweighting as discussed in the text. **b** The photoproduction MC (PHP) and the scaled tagged data are shown on a linear scale. The shaded area shows the uncertainty assigned to the photoproduction background, see Sect. 10.2

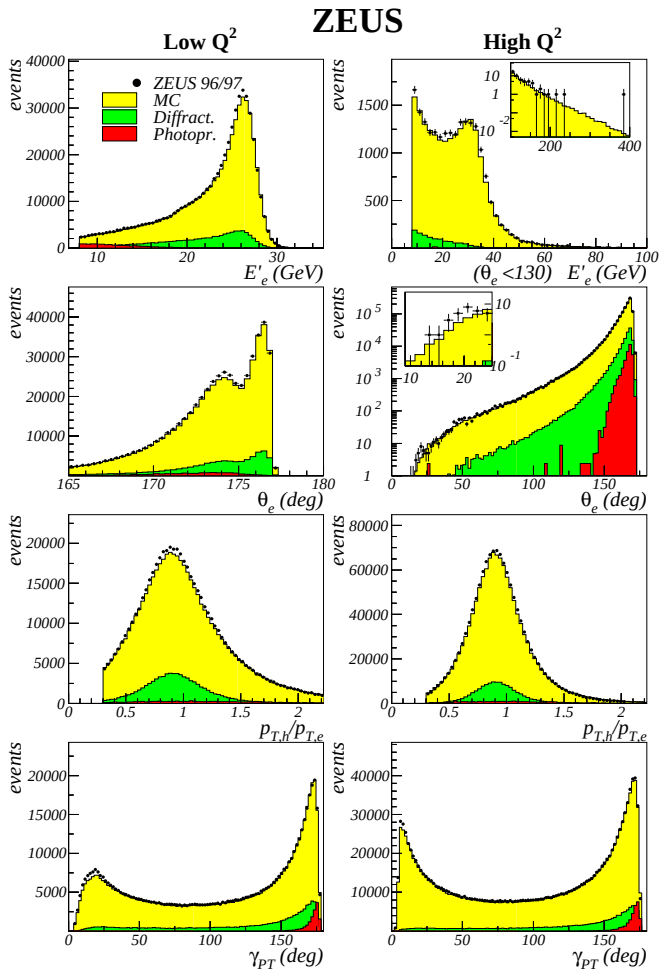

Fig. 5. Distributions of measured quantities, as discussed in the text, are shown for the low-Q^2 sample and the high-Q^2 sample. The MC histograms are based on the NLO QCD fit to the data and are normalised according to the luminosity. The diffractive component and the photoproduction background contributions are separately shown. The inserts show details of the corresponding distributions

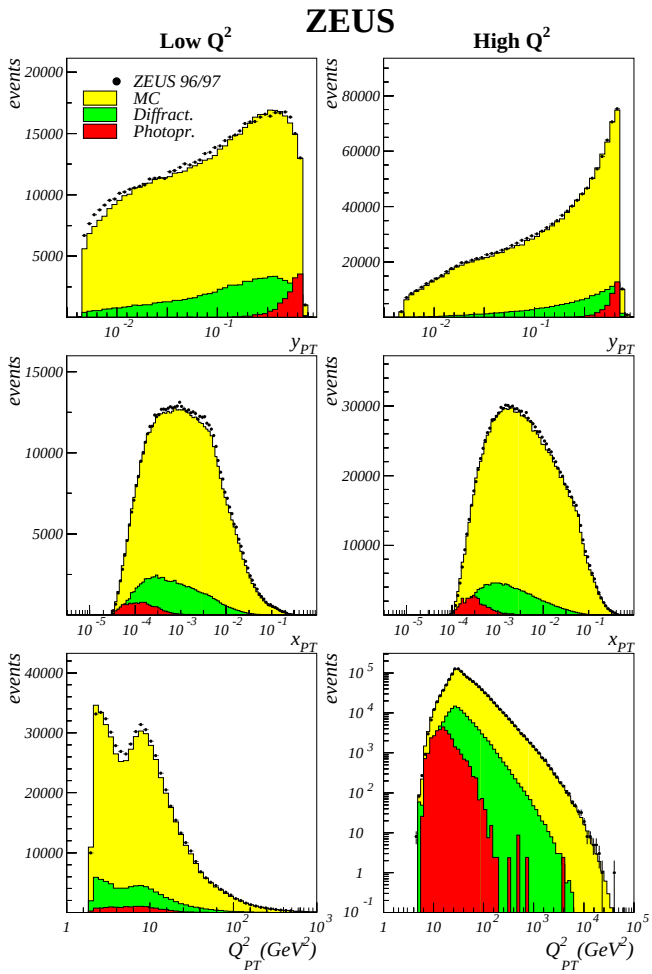

Fig. 6. Distributions of kinematic variables are shown for the low-Q^2 sample and the high-Q^2 sample. The MC histograms are based on the NLO QCD fit to the data and are normalised according to the luminosity. The diffractive component and the photoproduction background contributions are shown separately

region (see Sect. 10.2) is 10%. This discrepancy between data and MC simulation is approximately equal to the systematic uncertainty (not shown in the figure). Reweighting the MC simulation to get agreement in this region does not affect the extracted structure-function values.

10 Results

10.1 Extraction of the proton-structure function F_2^{em} and the reduced cross section

Monte Carlo events were generated according to (1) including QED radiative effects. The value of $\tilde{\sigma}^{e^+p}$, at fixed (x, Q^2) within a bin, was obtained from the ratio of the number of observed events to the number of events predicted from the MC simulation in that bin, multiplied by the reduced cross section from the Monte Carlo generator, $\tilde{\sigma}^{e^+p}_{\rm MC}(x, Q^2)$. The acceptance correction and bin-centering correction were thus taken from the MC simulation. The MC events contain transverse and longitudinal photon and Z^0 contributions, which can be written as F_2^{int}, F_2^{wk}, xF_3 and F_L or, equivalently, the *relative* corrections Δ_{F_2} (see (2)), Δ_{xF_3} and Δ_{F_L} according to:

$$\tilde{\sigma}^{e^+p} = F_2^{em}(1 + \Delta_{F_2} + \Delta_{xF_3} + \Delta_{F_L}) = F_2^{em}(1 + \Delta_{all}). \quad (7)$$

The result for F_2^{em} was obtained by correcting the reduced cross section, $\tilde{\sigma}^{e^+p}$, for these relative contributions, Δ_{all}, from the CTEQ4D parton distribution functions [34] used in the MC generation. The reduced cross section and F_2^{em} results do not significantly change if the NLO QCD fit results, instead of CTEQ4D, are used in the unfolding procedure.

The statistical uncertainties on the reduced cross sections were calculated from the number of events measured in the bins, taking into account the background and the statistical uncertainty from the MC simulation. Poisson statistics was used for the two bins that contain fewer than 5 events.

The reduced cross sections and F_2^{em} values were corrected for higher-order QED radiative effects not included in HERACLES. These second-order leading-logarithmic corrections, as well as third- and higher-order terms coming from soft-photon exponentiation, were evaluated using the program HECTOR 1.00 [35]. They lie between -0.2% and -0.5% and vary smoothly with Q^2. A constant correction of -0.35% was applied.

10.2 Systematic uncertainties

Several factors contribute to the systematic uncertainties of F_2^{em} and $\tilde{\sigma}^{e^+p}$. The relative uncertainties in $\tilde{\sigma}^{e^+p}$ are identical to those quoted for F_2^{em}. Ten sources of systematic uncertainties were found to be correlated between the different F_2^{em} bins and are denoted by {} in the text and in Table 2.

The ten correlated systematic uncertainties are:

{1} positron finding and efficiency.
The positron identification efficiency was varied within the uncertainty found in the QED Compton study, which is ∼2% for positron energies $E'_e \sim 8$ GeV and ∼1% for energies above 15 GeV. The effect on F_2^{em} is ∼1%, except in the lowest x bins where it reaches about 2%;

{2} positron scattering angle - A.
The uncertainty in the alignment of the different detector elements results in a systematic uncertainty in the angle of the scattered positron. The difference between the extrapolated track position at the face of the CAL and the position found from the CAL, the HES or the SRTD shows that this uncertainty was about 2 mm. The largest systematic uncertainty was obtained if the separation between the $+X$ and $-X$ halves of the RCAL was changed by ±2 mm, resulting in an uncertainty of $\sim 1\%$ for $Q^2 \lesssim 200$ GeV^2;

{3} positron scattering angle - B.
For positron angles measured with the tracking detector, the scattering angle θ_e was changed by the estimated systematic uncertainty of ±1 mrad in the track angle. This change had a 1% effect on the measured F_2^{em} at high Q^2;

{4} positron energy scale.
The systematic uncertainties in F_2^{em} due to the uncertainties in the absolute calorimeter-energy calibration for scattered positrons was estimated by changing the energy scale in the MC simulation: the change is 2% at 8 GeV, linearly decreasing to 1% at 15 GeV (see Sect. 7.2). Systematic variations of 1% in F_2^{em} are observed;

{5-7} hadronic energy measurement.
The hadronic energy scales of the different calorimeter regions in the MC simulation were changed by ±2% in turn for the FCAL {5}, BCAL {6} and RCAL {7}, while leaving the positron energy scale unchanged. The value of 2% is based on detailed comparisons of the distributions of the quantity $P_{T,h}/P_{T,e}$ from data and MC simulation, see Sect. 8. The effect on F_2^{em} was typically 2% in these bins at the highest or lowest y and about 0.5% elsewhere;

{8} hadronic energy flow - A.
The hadronic energy flow for diffractive events is different from that for non-diffractive events. To investigate the sensitivity of the PT reconstruction method to the size of the diffractive component, the diffractive scattering cross section in the MC simulation was reweighted such that it changed by ±50% while leaving the correction function $\mathcal{C}$ (5) unchanged. Effects of at most 2% at low Q^2 and high y in F_2^{em} were observed. The variations in F_2^{em} were negligible elsewhere. This is also a check on the effect of different simulations of the hadronic energy flow between the struck parton and the proton remnant;

Table 2. Relative uncertainties in the reduced cross section. The systematic uncertainties, denoted by the {}, are explained in Sect. 10.2. The overall normalisation uncertainty of 2% is not included, neither is the additional uncertainty of 1% at low Q^2

Q^2 (GeV^2)	x	$\tilde{\sigma}^{e^+p}$	δ_{stat} (%)	δ_{sys} (%)	δ_{unc} (%)	$\delta_{\{1\}}$ (%)	$\delta_{\{2\}}$ (%)	$\delta_{\{3\}}$ (%)	$\delta_{\{4\}}$ (%)	$\delta_{\{5\}}$ (%)	$\delta_{\{6\}}$ (%)	$\delta_{\{7\}}$ (%)	$\delta_{\{8\}}$ (%)	$\delta_{\{9\}}$ (%)	$\delta_{\{10\}}$ (%)
2.7	$6.32{\cdot}10^{-5}$	0.832	1.7	4.7	2.0	1.9	-0.1	0.0	0.2	0.1	0.2	1.4	1.9	2.9	0.3
2.7	$1.61{\cdot}10^{-4}$	0.740	1.0	2.4	1.8	1.4	0.3	0.0	-0.2	0.1	0.2	-0.3	0.1	0.4	-0.2
2.7	$4.00{\cdot}10^{-4}$	0.649	1.1	3.9	3.6	1.2	0.3	0.0	-0.3	0.1	0.4	-0.4	0.7	0.1	0.0
2.7	$6.32{\cdot}10^{-4}$	0.607	1.5	4.3	3.4	1.1	0.3	0.0	-0.5	0.6	-0.2	0.1	2.3	0.0	-0.1
2.7	$2.00{\cdot}10^{-3}$	0.477	0.9	4.2	2.7	1.1	0.1	0.0	-0.2	0.5	-0.1	-0.1	0.8	0.0	2.8
3.5	$6.32{\cdot}10^{-5}$	1.076	2.7	12.7	3.9	2.6	0.6	0.0	0.8	-0.1	0.4	2.6	4.3	10.6	0.1
3.5	$1.02{\cdot}10^{-4}$	0.951	2.0	3.6	2.0	1.7	0.3	0.0	0.7	0.1	0.1	0.8	0.8	1.9	0.1
3.5	$1.61{\cdot}10^{-4}$	0.882	2.0	2.5	1.9	1.4	0.1	0.0	0.3	-0.1	0.3	0.3	0.1	0.4	0.0
3.5	$2.53{\cdot}10^{-4}$	0.829	1.9	2.4	1.7	1.3	-0.4	0.0	-0.5	0.1	0.4	-0.6	-0.2	0.2	-0.2
3.5	$4.00{\cdot}10^{-4}$	0.787	1.9	2.7	2.1	1.2	-0.3	0.0	-0.4	-0.3	0.3	-0.5	0.8	0.0	0.3
3.5	$6.32{\cdot}10^{-4}$	0.700	1.9	3.0	2.5	1.1	0.2	0.0	0.4	0.3	0.3	-0.1	1.0	0.0	0.1
3.5	$2.00{\cdot}10^{-3}$	0.554	0.9	2.5	1.4	1.1	-0.1	0.0	-0.3	0.5	-0.1	0.0	0.8	0.0	1.5
3.5	$8.00{\cdot}10^{-3}$	0.472	1.0	6.3	1.6	1.1	-0.2	0.0	-0.5	0.7	-0.1	-0.1	-0.2	0.0	5.9
4.5	$1.02{\cdot}10^{-4}$	1.125	2.0	5.8	1.3	2.0	-0.4	0.0	0.3	-0.1	0.2	1.7	1.9	4.6	-0.1
4.5	$1.61{\cdot}10^{-4}$	0.994	2.0	2.2	0.7	1.6	0.6	0.0	0.3	0.1	0.2	0.3	0.7	0.7	0.0
4.5	$2.53{\cdot}10^{-4}$	0.923	2.0	2.6	1.9	1.3	0.0	0.0	-0.5	0.1	0.2	-0.3	1.1	0.1	0.0
4.5	$4.00{\cdot}10^{-4}$	0.882	2.2	2.4	1.9	1.2	-0.4	0.0	-0.4	-0.1	-0.2	-0.6	0.3	0.0	-0.3
4.5	$6.32{\cdot}10^{-4}$	0.803	2.2	2.0	1.4	1.2	-0.4	0.0	-0.1	0.2	0.3	-0.2	0.7	0.0	0.2
6.5	$1.02{\cdot}10^{-4}$	1.210	2.4	10.2	1.0	2.5	0.3	0.0	0.3	-0.2	0.5	2.5	2.4	9.2	0.2
6.5	$1.61{\cdot}10^{-4}$	1.159	1.5	3.6	0.4	1.8	0.0	0.0	0.6	0.1	0.1	0.6	0.9	2.8	0.0
6.5	$2.53{\cdot}10^{-4}$	1.078	1.5	1.9	0.5	1.5	0.4	0.0	0.5	0.1	0.3	0.3	0.5	0.6	0.0
6.5	$4.00{\cdot}10^{-4}$	0.972	1.5	1.8	0.9	1.3	-0.1	0.0	-0.4	-0.1	0.3	-0.6	-0.2	0.2	0.0
6.5	$6.32{\cdot}10^{-4}$	0.898	1.6	3.1	2.7	1.2	-0.2	0.0	-0.2	0.2	0.3	-0.4	0.4	0.0	0.0
6.5	$1.02{\cdot}10^{-3}$	0.828	1.6	2.1	1.6	1.1	0.3	0.0	-0.3	0.3	0.2	0.1	0.6	0.0	-0.1
6.5	$1.61{\cdot}10^{-3}$	0.740	1.8	2.5	2.0	1.1	-0.7	0.0	-0.4	-0.5	-0.3	-0.1	0.4	0.0	0.6
6.5	$2.53{\cdot}10^{-3}$	0.666	1.2	1.9	1.1	1.1	0.2	0.0	0.3	0.6	0.0	0.0	0.6	0.0	0.5
6.5	$5.00{\cdot}10^{-3}$	0.576	0.9	4.1	0.9	1.1	0.2	0.0	-0.3	0.4	0.0	0.1	0.0	0.0	3.9
6.5	$2.10{\cdot}10^{-2}$	0.487	1.2	8.7	1.9	1.1	-0.2	0.0	-0.7	0.8	-0.4	0.0	-0.5	0.0	8.3
8.5	$1.61{\cdot}10^{-4}$	1.212	2.5	9.9	1.7	2.4	0.6	0.0	-1.0	0.2	0.4	1.8	1.8	9.1	0.0
8.5	$2.53{\cdot}10^{-4}$	1.188	1.6	2.7	0.9	1.6	0.6	0.0	0.6	-0.1	0.2	0.4	0.2	1.6	0.2
8.5	$4.00{\cdot}10^{-4}$	1.067	1.6	2.0	0.9	1.4	0.6	0.0	-0.4	0.1	0.2	-0.4	0.1	0.6	-0.2
8.5	$6.32{\cdot}10^{-4}$	0.973	1.6	2.8	1.9	1.2	1.4	0.0	0.3	-0.1	0.4	-0.3	-0.2	0.1	0.3
8.5	$1.02{\cdot}10^{-3}$	0.875	1.6	1.6	0.8	1.2	-0.4	0.0	-0.4	-0.1	0.2	-0.3	0.0	0.1	-0.2
8.5	$1.61{\cdot}10^{-3}$	0.813	1.8	1.6	1.0	1.1	0.3	0.0	-0.1	0.3	0.0	-0.1	0.5	0.1	-0.3
10.0	$1.61{\cdot}10^{-4}$	1.230	4.2	12.8	1.4	2.7	-0.7	0.0	-0.6	-0.1	0.5	3.1	1.3	11.9	0.1
10.0	$2.53{\cdot}10^{-4}$	1.237	2.1	4.5	1.3	1.9	0.3	0.0	-0.3	-0.2	-0.1	0.7	-0.1	3.8	0.1
10.0	$4.00{\cdot}10^{-4}$	1.099	1.9	2.3	1.1	1.5	0.8	0.0	-0.2	0.1	0.3	-0.5	0.2	1.0	0.0
10.0	$6.32{\cdot}10^{-4}$	1.016	1.8	1.9	1.2	1.3	0.4	0.0	-0.1	-0.2	0.4	-0.6	-0.1	0.2	-0.1
10.0	$1.02{\cdot}10^{-3}$	0.934	1.8	1.9	1.3	1.2	0.2	0.0	-0.4	-0.2	0.2	-0.4	-0.2	0.0	0.0
10.0	$1.61{\cdot}10^{-3}$	0.851	2.1	2.0	1.2	1.1	1.1	0.0	0.2	-0.3	0.1	0.1	0.0	0.0	-0.1
10.0	$2.53{\cdot}10^{-3}$	0.761	2.0	2.4	1.8	1.1	0.9	0.0	-0.2	0.4	-0.2	-0.1	0.4	0.0	-0.4
10.0	$5.00{\cdot}10^{-3}$	0.624	1.1	2.9	0.8	1.1	0.8	0.0	-0.2	0.6	-0.1	0.0	0.1	0.0	2.4
10.0	$2.10{\cdot}10^{-2}$	0.503	1.1	6.8	1.3	1.0	0.7	0.0	-0.7	0.9	-0.2	0.1	-0.2	0.0	6.5
12.0	$2.53{\cdot}10^{-4}$	1.322	2.6	7.5	1.0	2.2	1.3	0.0	-1.0	0.2	0.3	1.0	0.5	6.8	0.2
12.0	$4.00{\cdot}10^{-4}$	1.191	2.3	2.7	0.9	1.6	0.6	0.0	0.2	-0.2	-0.1	0.1	0.3	1.9	0.0
12.0	$6.32{\cdot}10^{-4}$	1.070	2.1	2.3	1.6	1.3	0.3	0.0	-0.1	-0.2	0.2	-0.6	0.5	0.3	0.1
12.0	$1.02{\cdot}10^{-3}$	0.983	2.0	1.9	1.1	1.2	0.8	0.0	-0.2	0.2	0.4	-0.5	0.3	0.0	-0.1
12.0	$1.61{\cdot}10^{-3}$	0.899	2.2	1.6	0.7	1.1	0.8	0.0	-0.2	0.1	0.2	-0.1	0.1	0.1	0.1
12.0	$2.53{\cdot}10^{-3}$	0.793	2.1	1.9	1.0	1.1	0.6	0.0	0.4	0.3	-0.1	0.0	0.1	0.0	0.9
15.0	$2.53{\cdot}10^{-4}$	1.397	2.9	7.6	1.5	2.3	0.7	0.0	0.5	0.2	0.2	2.0	0.7	6.7	-0.1
15.0	$4.00{\cdot}10^{-4}$	1.258	2.3	3.7	1.5	1.8	0.4	0.0	-0.3	-0.2	0.3	0.1	0.8	2.7	0.0
15.0	$6.32{\cdot}10^{-4}$	1.137	2.0	2.2	0.9	1.4	1.0	0.0	-0.2	-0.1	0.3	-0.2	0.3	0.8	-0.2
15.0	$1.02{\cdot}10^{-3}$	1.055	1.9	1.9	1.1	1.2	0.3	0.0	-0.2	-0.3	0.3	-0.6	0.2	0.1	0.1
15.0	$1.61{\cdot}10^{-3}$	0.944	2.2	1.6	0.7	1.2	0.6	0.0	-0.5	0.1	0.0	-0.2	0.1	0.0	-0.1

Table 2. (continued)

Q^2 (GeV^2)	x	$\tilde{\sigma}^{e^+p}$	δ_{stat} (%)	δ_{sys} (%)	δ_{unc} (%)	$\delta_{\{1\}}$ (%)	$\delta_{\{2\}}$ (%)	$\delta_{\{3\}}$ (%)	$\delta_{\{4\}}$ (%)	$\delta_{\{5\}}$ (%)	$\delta_{\{6\}}$ (%)	$\delta_{\{7\}}$ (%)	$\delta_{\{8\}}$ (%)	$\delta_{\{9\}}$ (%)	$\delta_{\{10\}}$ (%)
15.0	$2.53{\cdot}10^{-3}$	0.836	2.1	1.6	0.9	1.1	0.6	0.0	-0.3	0.3	-0.1	-0.1	0.1	0.0	-0.2
15.0	$5.00{\cdot}10^{-3}$	0.706	1.5	1.5	0.8	1.1	0.3	0.0	-0.1	0.5	-0.1	0.0	0.2	0.0	0.1
15.0	$2.10{\cdot}10^{-2}$	0.519	1.0	6.9	1.0	1.0	0.7	0.0	-0.6	0.5	-0.2	0.1	-0.2	0.0	6.6
18.0	$5.00{\cdot}10^{-4}$	1.284	1.9	4.1	0.7	1.9	0.4	0.0	-0.5	0.1	0.3	0.4	0.2	3.5	0.1
18.0	$8.00{\cdot}10^{-4}$	1.157	2.2	2.4	0.9	1.4	1.4	0.0	-0.1	-0.1	0.3	-0.6	0.1	0.5	0.3
18.0	$1.30{\cdot}10^{-3}$	1.038	2.0	2.2	1.5	1.2	0.8	0.0	-0.3	-0.1	0.4	-0.4	0.3	0.1	0.1
18.0	$2.10{\cdot}10^{-3}$	0.929	2.3	1.6	0.9	1.1	0.2	0.0	0.0	-0.2	-0.2	-0.2	0.4	0.0	-0.5
18.0	$3.20{\cdot}10^{-3}$	0.851	2.4	1.8	1.0	1.1	0.9	0.0	-0.5	0.2	0.2	0.1	0.2	0.1	0.2
18.0	$5.00{\cdot}10^{-3}$	0.739	1.7	1.7	0.6	1.1	0.9	0.0	-0.2	0.4	-0.2	0.0	-0.1	0.0	0.6
22.0	$5.00{\cdot}10^{-4}$	1.357	2.5	4.0	1.2	2.0	0.5	0.0	-1.0	0.1	0.2	0.6	0.7	2.8	0.0
22.0	$8.00{\cdot}10^{-4}$	1.267	2.2	1.9	0.6	1.5	-0.1	0.0	0.3	-0.1	0.3	-0.1	0.3	0.6	-0.5
22.0	$1.30{\cdot}10^{-3}$	1.065	2.3	2.3	1.4	1.3	1.0	0.0	-0.1	-0.2	0.4	-0.5	0.0	0.2	0.1
22.0	$2.10{\cdot}10^{-3}$	1.001	2.7	2.0	0.8	1.2	0.8	0.0	-1.0	0.2	-0.3	-0.2	0.3	0.0	-0.1
22.0	$3.20{\cdot}10^{-3}$	0.905	2.6	1.7	1.2	1.1	0.3	0.0	0.1	-0.4	0.1	-0.1	0.3	0.1	0.1
22.0	$5.00{\cdot}10^{-3}$	0.771	2.4	1.7	0.9	1.1	0.4	0.0	-0.3	0.3	-0.2	-0.1	0.2	0.0	-0.7
22.0	$8.00{\cdot}10^{-3}$	0.656	2.4	1.7	0.9	1.1	0.4	0.0	-0.7	0.5	-0.3	0.0	0.3	0.0	0.1
22.0	$1.30{\cdot}10^{-2}$	0.581	2.0	5.6	1.8	1.0	0.9	0.0	-0.3	0.4	0.1	-0.1	0.0	0.0	5.1
22.0	$3.20{\cdot}10^{-2}$	0.512	1.8	6.9	1.6	1.0	0.9	0.0	-0.7	1.4	-0.3	0.1	-0.3	0.0	6.4
27.0	$5.00{\cdot}10^{-4}$	1.497	3.3	4.0	1.5	2.1	0.7	0.0	0.1	0.2	0.2	1.3	0.9	2.5	0.3
27.0	$8.00{\cdot}10^{-4}$	1.294	2.5	2.2	0.8	1.7	0.4	0.0	0.1	0.1	0.3	0.2	0.4	0.9	0.0
27.0	$1.30{\cdot}10^{-3}$	1.181	2.3	2.7	1.8	1.4	1.1	0.0	-0.2	0.1	0.2	-0.6	0.1	0.2	0.0
27.0	$2.10{\cdot}10^{-3}$	1.095	2.8	1.7	1.0	1.2	0.5	0.0	0.2	-0.1	0.3	-0.2	0.0	0.1	0.0
27.0	$3.20{\cdot}10^{-3}$	0.901	2.7	2.1	1.5	1.2	0.8	0.0	0.1	0.2	-0.2	0.0	0.5	0.1	0.0
27.0	$5.00{\cdot}10^{-3}$	0.804	2.5	2.5	1.5	1.1	1.0	0.0	-1.1	0.2	-0.5	-0.1	0.3	0.0	-0.2
27.0	$8.00{\cdot}10^{-3}$	0.731	2.6	2.7	1.3	1.1	1.2	0.0	-0.4	0.7	-0.2	0.1	0.1	0.0	1.4
27.0	$1.30{\cdot}10^{-2}$	0.634	2.0	2.9	1.4	1.0	0.6	0.0	-0.4	0.3	0.0	0.1	-0.1	0.0	2.2
35.0	$8.00{\cdot}10^{-4}$	1.404	1.5	2.9	0.7	1.9	0.4	0.0	-1.0	0.0	0.0	0.3	1.1	1.4	0.0
35.0	$1.30{\cdot}10^{-3}$	1.225	1.4	1.8	0.3	1.5	0.5	0.0	-0.3	-0.1	0.4	-0.5	0.3	0.3	0.1
35.0	$2.10{\cdot}10^{-3}$	1.108	1.6	1.6	0.4	1.3	0.6	0.0	-0.5	-0.1	0.3	-0.4	0.1	0.0	-0.1
35.0	$3.20{\cdot}10^{-3}$	0.961	1.7	1.6	0.7	1.2	0.6	0.0	0.3	0.1	0.1	-0.1	-0.4	0.0	-0.2
35.0	$5.00{\cdot}10^{-3}$	0.864	1.6	1.5	0.4	1.1	0.6	0.0	-0.6	0.2	0.1	0.1	-0.1	0.0	-0.1
35.0	$8.00{\cdot}10^{-3}$	0.727	1.6	1.8	0.7	1.1	0.7	0.0	-0.4	0.5	-0.4	0.0	0.1	0.0	-0.6
35.0	$1.30{\cdot}10^{-2}$	0.646	1.9	2.2	0.9	1.1	0.5	0.0	-0.3	0.9	-0.1	-0.1	0.0	0.0	1.4
35.0	$2.10{\cdot}10^{-2}$	0.555	1.8	2.8	1.1	1.0	1.0	0.0	-0.5	-0.3	-0.2	0.2	-0.2	0.0	2.0
35.0	$3.20{\cdot}10^{-2}$	0.496	1.1	7.6	1.0	1.0	0.9	0.0	-1.2	0.9	-0.2	0.1	-0.2	0.0	7.2
45.0	$8.00{\cdot}10^{-4}$	1.482	1.8	3.6	1.4	2.0	0.4	0.0	0.3	-0.1	0.3	1.6	0.1	1.9	0.0
45.0	$1.30{\cdot}10^{-3}$	1.297	1.3	2.1	0.3	1.6	0.5	0.0	-0.7	0.0	0.3	-0.8	0.2	0.4	0.0
45.0	$2.10{\cdot}10^{-3}$	1.131	1.7	1.7	0.4	1.4	0.5	0.0	-0.2	0.1	0.6	-0.3	-0.1	0.1	0.1
45.0	$3.20{\cdot}10^{-3}$	0.998	1.5	1.5	0.5	1.2	0.6	0.0	-0.2	0.2	0.1	-0.2	0.0	0.0	-0.2
45.0	$5.00{\cdot}10^{-3}$	0.909	1.4	1.3	0.4	1.2	0.2	0.0	-0.2	0.2	0.1	-0.2	-0.2	0.0	0.1
45.0	$8.00{\cdot}10^{-3}$	0.777	1.4	1.5	0.4	1.1	0.5	0.0	-0.5	-0.4	-0.3	-0.1	0.3	0.0	0.1
45.0	$1.30{\cdot}10^{-2}$	0.661	1.7	1.7	0.8	1.1	0.2	0.0	-0.8	0.6	-0.2	-0.1	-0.1	0.0	-0.1
45.0	$2.10{\cdot}10^{-2}$	0.587	1.7	2.1	0.3	1.0	0.4	0.0	-0.6	0.3	0.0	0.1	-0.3	0.0	1.6
60.0	$1.30{\cdot}10^{-3}$	1.387	1.3	2.2	0.6	1.8	0.5	-0.1	-0.4	0.1	0.1	-0.1	0.4	0.7	0.0
60.0	$2.10{\cdot}10^{-3}$	1.213	1.5	1.8	0.5	1.5	0.4	0.0	-0.2	-0.2	0.4	-0.4	0.4	0.4	-0.1
60.0	$3.20{\cdot}10^{-3}$	1.074	1.5	1.5	0.4	1.3	0.4	0.0	0.2	-0.1	0.4	-0.3	-0.2	0.1	-0.1
60.0	$5.00{\cdot}10^{-3}$	0.900	1.4	1.5	0.5	1.2	0.4	0.0	0.4	0.2	0.3	-0.1	0.2	0.0	0.1
60.0	$8.00{\cdot}10^{-3}$	0.809	1.4	1.5	0.7	1.1	0.5	0.0	-0.6	0.2	-0.3	0.1	0.2	0.0	0.1
60.0	$1.30{\cdot}10^{-2}$	0.689	1.7	1.9	0.8	1.1	0.7	0.0	-0.6	0.7	-0.3	0.1	0.2	0.0	-0.5
60.0	$2.10{\cdot}10^{-2}$	0.598	1.6	2.4	1.1	1.1	0.6	0.0	-0.7	0.2	-0.1	0.1	0.0	0.0	1.5
60.0	$3.20{\cdot}10^{-2}$	0.537	2.0	3.3	1.3	1.0	0.5	0.0	-0.6	0.7	0.0	0.2	-0.2	0.0	2.7
60.0	$5.00{\cdot}10^{-2}$	0.512	1.5	6.8	1.9	1.0	0.0	0.0	-0.8	0.9	-0.3	-0.1	-0.1	0.0	6.3

Table 2. (continued)

Q^2 (GeV^2)	x	$\tilde{\sigma}^{e^+p}$	δ_{stat} (%)	δ_{sys} (%)	δ_{unc} (%)	$\delta_{\{1\}}$ (%)	$\delta_{\{2\}}$ (%)	$\delta_{\{3\}}$ (%)	$\delta_{\{4\}}$ (%)	$\delta_{\{5\}}$ (%)	$\delta_{\{6\}}$ (%)	$\delta_{\{7\}}$ (%)	$\delta_{\{8\}}$ (%)	$\delta_{\{9\}}$ (%)	$\delta_{\{10\}}$ (%)
70.0	$1.30{\cdot}10^{-3}$	1.438	1.8	2.2	0.6	1.9	0.3	-0.3	-0.5	0.1	0.1	0.3	-0.3	0.5	0.0
70.0	$2.10{\cdot}10^{-3}$	1.238	1.7	1.9	0.3	1.6	0.4	-0.1	0.3	0.1	0.4	-0.3	0.4	0.5	0.1
70.0	$3.20{\cdot}10^{-3}$	1.087	1.7	1.6	0.5	1.4	0.5	0.0	-0.2	-0.1	0.3	-0.3	0.0	0.1	-0.1
70.0	$5.00{\cdot}10^{-3}$	0.984	1.5	1.5	0.4	1.2	0.5	0.0	-0.3	0.2	0.2	-0.1	-0.2	0.0	0.2
70.0	$8.00{\cdot}10^{-3}$	0.815	1.6	1.4	0.5	1.1	0.2	0.0	-0.4	0.2	0.1	-0.1	-0.2	0.0	-0.3
70.0	$1.30{\cdot}10^{-2}$	0.708	1.9	1.7	0.5	1.1	0.3	0.0	-0.6	0.8	-0.3	-0.1	0.2	0.0	-0.4
70.0	$2.10{\cdot}10^{-2}$	0.620	1.8	1.6	0.7	1.1	0.4	0.0	-0.6	0.6	-0.2	0.1	0.0	0.0	0.5
70.0	$3.20{\cdot}10^{-2}$	0.557	2.1	2.8	0.9	1.0	0.3	0.0	-0.3	-0.2	0.3	-0.1	-0.2	0.0	2.3
70.0	$5.00{\cdot}10^{-2}$	0.500	1.6	6.2	0.9	1.0	0.3	0.0	-0.7	0.5	-0.2	0.2	-0.1	0.0	6.0
90.0	$2.10{\cdot}10^{-3}$	1.236	2.0	2.2	0.4	1.8	0.2	-0.4	-0.8	0.0	0.4	-0.2	0.2	0.5	0.0
90.0	$3.20{\cdot}10^{-3}$	1.168	1.9	1.7	0.2	1.5	0.4	-0.3	0.3	0.1	0.4	-0.2	-0.1	0.0	0.1
90.0	$5.00{\cdot}10^{-3}$	1.029	1.7	1.7	0.6	1.3	0.2	-0.1	-0.7	-0.1	0.1	-0.2	-0.3	0.0	-0.3
90.0	$8.00{\cdot}10^{-3}$	0.896	1.8	1.5	0.2	1.2	0.7	0.0	-0.4	-0.2	-0.1	-0.2	0.0	0.0	0.1
90.0	$1.30{\cdot}10^{-2}$	0.749	2.1	1.6	1.0	1.1	0.4	0.0	-0.2	0.3	-0.3	-0.1	0.2	0.0	0.1
90.0	$2.10{\cdot}10^{-2}$	0.622	1.9	1.9	0.6	1.1	0.4	0.0	-0.3	0.9	-0.3	0.2	0.1	0.0	-1.0
90.0	$3.20{\cdot}10^{-2}$	0.535	2.3	2.9	1.2	1.0	0.6	0.0	-0.3	0.5	0.2	0.0	-0.1	0.0	2.2
90.0	$5.00{\cdot}10^{-2}$	0.484	2.1	6.3	0.9	1.0	0.2	0.0	0.2	0.1	0.2	0.1	-0.2	0.0	6.1
90.0	$8.00{\cdot}10^{-2}$	0.435	2.0	2.8	0.9	1.0	0.2	0.0	-0.6	0.7	-0.1	0.1	0.0	0.0	2.3
90.0	$1.80{\cdot}10^{-1}$	0.340	3.1	5.3	3.0	1.0	0.7	0.0	-3.1	1.6	-1.4	-0.7	0.0	0.0	-1.8
120.0	$2.10{\cdot}10^{-3}$	1.317	2.2	2.5	0.8	2.0	0.0	0.6	-0.9	0.1	0.1	0.3	-0.6	0.0	-0.1
120.0	$3.20{\cdot}10^{-3}$	1.173	1.9	2.0	0.7	1.7	0.3	0.1	-0.7	0.0	0.3	-0.4	0.0	0.1	0.0
120.0	$5.00{\cdot}10^{-3}$	1.038	1.7	1.8	0.5	1.4	0.5	-0.7	0.1	-0.2	0.4	-0.2	-0.2	0.1	0.0
120.0	$8.00{\cdot}10^{-3}$	0.908	1.8	1.4	0.4	1.2	0.4	-0.3	-0.1	0.1	0.0	-0.1	-0.1	0.0	0.0
120.0	$1.30{\cdot}10^{-2}$	0.760	2.0	1.8	0.5	1.1	0.3	0.0	-1.1	0.2	-0.2	-0.1	-0.1	0.0	0.4
120.0	$2.10{\cdot}10^{-2}$	0.664	1.9	1.8	0.7	1.1	0.4	-0.1	-0.2	1.0	-0.4	0.1	-0.2	0.0	-0.2
120.0	$3.20{\cdot}10^{-2}$	0.579	2.3	2.2	0.9	1.0	0.4	0.0	-0.5	0.1	0.1	0.4	-0.1	0.0	-1.5
120.0	$5.00{\cdot}10^{-2}$	0.472	2.1	5.1	0.8	1.0	0.7	0.0	0.1	-0.3	-0.3	0.1	-0.1	0.0	4.9
120.0	$8.00{\cdot}10^{-2}$	0.437	1.9	4.7	0.7	1.0	0.4	0.0	-0.9	0.6	-0.2	0.0	-0.1	0.0	4.4
120.0	$1.80{\cdot}10^{-1}$	0.328	2.7	8.8	3.2	1.0	0.6	0.0	-2.2	-1.3	-0.9	-0.6	0.0	0.0	-7.6
150.0	$3.20{\cdot}10^{-3}$	1.194	2.1	2.3	0.6	1.9	0.0	0.4	-0.9	-0.1	0.1	0.3	-0.5	0.1	0.0
150.0	$5.00{\cdot}10^{-3}$	1.037	1.9	1.8	0.5	1.5	0.1	0.4	-0.2	0.1	0.5	-0.3	-0.3	0.0	-0.1
150.0	$8.00{\cdot}10^{-3}$	0.887	1.8	1.6	0.7	1.3	0.3	-0.3	-0.4	0.1	-0.2	0.1	-0.2	0.0	0.0
150.0	$1.30{\cdot}10^{-2}$	0.805	2.1	2.0	0.5	1.2	0.4	-1.0	-1.0	0.2	-0.2	-0.1	-0.3	0.0	-0.3
150.0	$2.10{\cdot}10^{-2}$	0.661	2.0	1.9	0.6	1.1	0.5	-0.7	-0.4	0.7	-0.4	0.1	0.0	0.0	0.7
150.0	$3.20{\cdot}10^{-2}$	0.574	2.4	1.7	0.7	1.0	0.3	-0.7	0.0	0.7	-0.2	-0.1	-0.3	0.0	0.3
150.0	$5.00{\cdot}10^{-2}$	0.515	2.2	2.3	1.3	1.0	0.6	-0.5	-0.5	-0.4	0.2	0.2	-0.1	0.0	1.3
150.0	$8.00{\cdot}10^{-2}$	0.431	2.0	5.0	1.0	1.0	0.5	-0.5	-0.4	0.6	0.1	0.1	-0.1	0.0	4.7
150.0	$1.80{\cdot}10^{-1}$	0.326	2.7	6.4	2.3	1.0	0.5	-0.5	-2.5	-1.3	-1.0	-0.4	0.0	0.0	-5.0
200.0	$3.20{\cdot}10^{-3}$	1.162	3.8	3.2	2.0	2.0	0.0	0.8	-1.2	0.2	0.3	0.4	-0.4	0.1	0.0
200.0	$5.00{\cdot}10^{-3}$	1.065	2.3	2.1	0.4	1.7	0.0	0.6	-0.8	-0.1	0.4	-0.3	0.0	0.0	0.2
200.0	$8.00{\cdot}10^{-3}$	0.899	2.2	1.8	0.6	1.4	0.1	0.5	0.6	0.1	0.4	-0.2	0.1	0.0	0.0
200.0	$1.30{\cdot}10^{-2}$	0.794	2.2	1.5	0.2	1.2	0.1	0.3	-0.5	0.2	-0.5	0.0	-0.1	0.0	-0.2
200.0	$2.10{\cdot}10^{-2}$	0.659	2.7	1.8	0.7	1.1	-0.1	0.7	0.5	0.4	-0.7	-0.1	-0.1	0.0	0.1
200.0	$3.20{\cdot}10^{-2}$	0.570	2.8	1.9	0.5	1.1	0.0	0.3	-0.8	0.7	-0.5	0.2	0.0	0.0	0.9
200.0	$5.00{\cdot}10^{-2}$	0.508	2.8	2.4	0.5	1.0	0.3	-0.3	-0.6	-0.4	-0.2	-0.2	-0.1	0.0	2.0
200.0	$8.00{\cdot}10^{-2}$	0.434	2.4	2.7	0.5	1.0	-0.3	-0.7	0.1	0.4	0.4	0.3	-0.1	0.0	2.3
200.0	$1.80{\cdot}10^{-1}$	0.340	2.9	3.7	0.6	1.0	0.3	-0.1	-2.4	-1.2	-0.9	-0.3	0.0	0.0	-1.9
250.0	$5.00{\cdot}10^{-3}$	1.066	3.0	2.9	1.3	1.9	0.0	0.6	-1.6	0.1	0.4	-0.2	0.1	0.0	0.0
250.0	$8.00{\cdot}10^{-3}$	0.927	2.6	1.7	0.5	1.5	0.0	0.5	-0.2	-0.1	0.4	-0.2	-0.1	0.0	0.0
250.0	$1.30{\cdot}10^{-2}$	0.821	2.7	1.8	0.9	1.3	0.0	0.4	0.5	0.3	0.5	0.1	-0.1	0.0	0.4
250.0	$2.10{\cdot}10^{-2}$	0.644	3.5	1.8	0.6	1.1	0.0	-0.4	-0.8	-0.3	-0.3	-0.2	0.0	0.0	-0.7
250.0	$3.20{\cdot}10^{-2}$	0.612	3.4	2.3	1.0	1.1	0.1	0.9	-0.7	0.9	-1.0	0.0	0.1	0.0	-0.3

Table 2. (continued)

Q^2 (GeV^2)	x	$\tilde{\sigma}^{e^+p}$	δ_{stat} (%)	δ_{sys} (%)	δ_{unc} (%)	$\delta_{\{1\}}$ (%)	$\delta_{\{2\}}$ (%)	$\delta_{\{3\}}$ (%)	$\delta_{\{4\}}$ (%)	$\delta_{\{5\}}$ (%)	$\delta_{\{6\}}$ (%)	$\delta_{\{7\}}$ (%)	$\delta_{\{8\}}$ (%)	$\delta_{\{9\}}$ (%)	$\delta_{\{10\}}$ (%)
250.0	$5.00\cdot10^{-2}$	0.517	3.2	1.8	1.1	1.0	0.1	0.5	0.3	0.4	-0.1	0.1	-0.2	0.0	-0.3
250.0	$8.00\cdot10^{-2}$	0.445	2.8	5.1	0.3	1.0	0.1	1.0	-0.6	-0.2	0.2	-0.3	-0.1	0.0	4.8
250.0	$1.80\cdot10^{-1}$	0.341	3.2	5.6	1.1	1.0	0.1	0.5	-1.0	1.3	-0.2	0.3	0.0	0.0	-5.1
350.0	$5.00\cdot10^{-3}$	1.103	4.4	3.5	2.7	2.0	0.0	-0.2	-0.6	-0.2	0.3	0.4	0.0	0.0	-0.2
350.0	$8.00\cdot10^{-3}$	0.988	2.9	2.1	0.4	1.7	0.0	0.2	-0.8	-0.1	0.8	0.1	-0.4	0.0	-0.2
350.0	$1.30\cdot10^{-2}$	0.824	2.9	1.7	0.5	1.3	0.0	0.7	-0.3	-0.1	0.1	-0.1	-0.3	0.0	0.0
350.0	$2.10\cdot10^{-2}$	0.679	3.6	1.9	1.1	1.2	0.0	0.8	-0.4	0.2	-0.4	-0.1	0.0	0.0	0.0
350.0	$3.20\cdot10^{-2}$	0.639	3.6	2.0	0.8	1.1	0.0	0.6	0.5	0.8	-0.8	0.1	-0.2	0.0	-0.5
350.0	$5.00\cdot10^{-2}$	0.526	3.4	1.9	0.6	1.0	0.0	0.8	-0.8	0.3	-0.5	-0.1	-0.1	0.0	0.8
350.0	$8.00\cdot10^{-2}$	0.442	3.2	2.6	0.6	1.0	0.0	0.5	-0.7	-0.5	-0.2	0.0	-0.1	0.0	2.1
350.0	$1.80\cdot10^{-1}$	0.328	3.5	1.6	0.4	1.0	0.0	0.2	-0.8	0.6	-0.3	0.3	0.0	0.0	-0.3
450.0	$8.00\cdot10^{-3}$	0.954	3.5	2.4	1.4	1.8	0.0	-0.2	-0.1	-0.1	0.6	-0.1	-0.1	0.3	-0.1
450.0	$1.30\cdot10^{-2}$	0.854	3.0	1.7	0.6	1.4	0.0	0.4	-0.4	0.1	0.3	-0.1	-0.1	0.0	0.1
450.0	$2.10\cdot10^{-2}$	0.702	3.6	1.6	0.8	1.2	0.0	0.2	0.5	0.1	0.2	0.1	0.1	0.0	0.2
450.0	$3.20\cdot10^{-2}$	0.579	4.3	1.8	0.3	1.1	0.0	0.7	-0.7	0.7	-0.6	-0.1	0.0	0.0	-0.5
450.0	$5.00\cdot10^{-2}$	0.511	3.4	1.5	0.5	1.0	0.0	0.3	-0.4	0.6	-0.5	0.1	-0.3	0.0	0.0
450.0	$8.00\cdot10^{-2}$	0.439	3.6	2.3	1.1	1.0	0.0	0.5	-0.5	-0.7	-0.1	0.0	-0.1	0.0	1.3
450.0	$1.30\cdot10^{-1}$	0.365	3.8	2.3	1.0	1.0	0.0	0.9	-0.2	0.2	0.2	0.1	0.0	0.0	1.6
450.0	$2.50\cdot10^{-1}$	0.264	4.5	7.7	1.7	1.0	0.0	0.9	-2.4	-0.8	-0.7	-0.3	0.0	0.0	-6.9
650.0	$8.00\cdot10^{-3}$	0.926	4.6	3.2	1.8	1.9	0.0	0.2	-1.5	-0.1	0.0	0.5	-0.7	0.0	0.0
650.0	$1.30\cdot10^{-2}$	0.827	3.3	1.9	0.7	1.5	0.0	0.4	-0.3	-0.1	0.6	-0.2	-0.2	0.1	0.1
650.0	$2.10\cdot10^{-2}$	0.722	3.8	1.7	0.9	1.2	0.0	0.4	-0.5	0.2	0.3	0.0	0.1	0.0	-0.1
650.0	$3.20\cdot10^{-2}$	0.603	4.0	1.9	0.9	1.1	0.0	0.3	-0.4	0.2	-0.1	0.1	0.1	0.0	1.1
650.0	$5.00\cdot10^{-2}$	0.475	4.3	2.1	1.0	1.0	0.0	0.4	-0.4	1.1	-0.9	-0.1	0.0	0.0	-0.2
650.0	$8.00\cdot10^{-2}$	0.456	3.9	1.5	0.8	1.0	0.0	-0.3	-0.4	-0.3	0.1	0.2	-0.1	0.0	0.6
650.0	$1.30\cdot10^{-1}$	0.357	4.2	3.2	1.4	1.0	0.0	0.3	-0.8	0.3	0.2	0.1	0.0	0.0	2.5
650.0	$2.50\cdot10^{-1}$	0.250	4.8	3.4	1.7	1.0	0.0	0.7	-1.8	-0.4	-0.6	-0.1	0.0	0.0	1.8
650.0	$4.00\cdot10^{-1}$	0.152	9.5	14.5	0.8	1.0	0.0	1.1	-5.6	-3.9	-1.3	-1.3	0.0	0.0	-12.5
800.0	$1.30\cdot10^{-2}$	0.847	4.5	2.4	1.0	1.7	0.0	0.3	-1.0	0.0	0.4	-0.2	-0.4	0.0	-0.4
800.0	$2.10\cdot10^{-2}$	0.665	7.5	1.6	0.6	1.3	0.0	0.1	0.6	-0.1	0.4	-0.2	0.1	0.0	-0.4
800.0	$3.20\cdot10^{-2}$	0.647	4.9	1.4	0.6	1.1	0.0	0.5	-0.4	-0.1	-0.3	0.0	-0.1	0.0	-0.2
800.0	$5.00\cdot10^{-2}$	0.451	5.0	2.3	1.3	1.0	0.0	0.3	0.3	1.1	-0.8	0.0	0.0	0.0	0.6
800.0	$8.00\cdot10^{-2}$	0.420	5.8	2.6	1.0	1.0	0.0	0.9	-1.4	0.6	-0.4	-0.1	0.0	0.0	1.2
800.0	$1.30\cdot10^{-1}$	0.370	5.2	2.5	0.8	1.0	0.0	0.6	-0.7	-0.5	0.0	-0.1	0.0	0.0	-1.9
800.0	$2.50\cdot10^{-1}$	0.260	5.9	1.8	0.4	1.0	0.0	-0.1	-0.5	0.3	-0.2	0.2	0.0	0.0	1.3
800.0	$4.00\cdot10^{-1}$	0.114	11.4	13.5	2.2	1.0	0.0	0.8	-5.3	-3.1	-0.8	-0.8	0.0	0.0	-11.7
1200.0	$1.40\cdot10^{-2}$	0.872	5.5	2.9	1.1	1.7	0.0	0.2	-2.0	0.1	0.5	0.3	-0.3	0.0	0.0
1200.0	$2.10\cdot10^{-2}$	0.681	5.1	1.8	0.8	1.3	0.0	0.2	-0.6	-0.1	0.5	-0.1	0.3	0.0	0.0
1200.0	$3.20\cdot10^{-2}$	0.563	5.0	2.0	1.5	1.1	0.0	0.3	0.5	0.2	0.1	0.1	0.2	0.0	-0.1
1200.0	$5.00\cdot10^{-2}$	0.490	4.6	1.6	1.0	1.0	0.0	0.4	-0.2	0.4	-0.2	-0.2	-0.1	0.0	-0.2
1200.0	$8.00\cdot10^{-2}$	0.434	5.3	1.5	0.4	1.0	0.0	-0.1	-0.3	0.7	-0.6	0.2	-0.2	0.0	-0.1
1200.0	$1.30\cdot10^{-1}$	0.336	5.8	3.1	0.6	1.0	0.0	0.3	-0.6	0.5	0.1	-0.1	0.0	0.0	2.8
1200.0	$2.50\cdot10^{-1}$	0.254	5.4	2.0	1.0	1.0	0.0	0.5	-1.3	-0.3	-0.1	0.1	0.0	0.0	0.1
1200.0	$4.00\cdot10^{-1}$	0.149	8.1	10.3	2.9	1.0	0.0	0.3	-3.1	-2.4	-0.7	-0.2	0.0	0.0	-9.0
1200.0	$6.50\cdot10^{-1}$	0.021	35.6	25.1	17.5	1.0	0.0	-0.9	-13.3	-5.3	-1.5	-2.2	0.0	0.0	-10.5
1500.0	$2.10\cdot10^{-2}$	0.666	7.9	6.2	5.8	1.5	0.0	0.3	1.0	0.0	0.3	-0.4	0.2	0.0	-0.5
1500.0	$3.20\cdot10^{-2}$	0.540	10.3	2.0	1.3	1.1	0.0	0.2	-0.2	0.2	0.5	0.0	0.3	0.0	-0.8
1500.0	$5.00\cdot10^{-2}$	0.518	5.8	1.8	1.1	1.0	0.0	0.3	-0.4	-0.2	-0.2	-0.1	-0.4	0.0	0.5
1500.0	$8.00\cdot10^{-2}$	0.476	5.7	2.6	1.0	1.0	0.0	0.5	-0.6	0.8	-1.0	-0.1	0.1	0.0	-1.6
1500.0	$1.30\cdot10^{-1}$	0.301	11.8	1.9	1.2	1.0	0.0	0.2	0.1	-0.1	-0.3	0.2	0.0	0.0	1.0
1500.0	$1.80\cdot10^{-1}$	0.313	7.3	5.9	1.2	1.0	0.0	0.2	-0.9	0.6	0.3	-0.1	0.0	0.0	5.6
1500.0	$2.50\cdot10^{-1}$	0.270	8.6	3.0	2.2	1.0	0.0	0.1	-1.7	-0.5	-0.1	0.1	0.0	0.0	0.0

Table 2. (continued)

Q^2 (GeV^2)	x	$\tilde{\sigma}^{e^+p}$	δ_{stat} (%)	δ_{sys} (%)	δ_{unc} (%)	$\delta_{\{1\}}$ (%)	$\delta_{\{2\}}$ (%)	$\delta_{\{3\}}$ (%)	$\delta_{\{4\}}$ (%)	$\delta_{\{5\}}$ (%)	$\delta_{\{6\}}$ (%)	$\delta_{\{7\}}$ (%)	$\delta_{\{8\}}$ (%)	$\delta_{\{9\}}$ (%)	$\delta_{\{10\}}$ (%)
1500.0	$4.00{\cdot}10^{-1}$	0.146	12.6	13.7	1.9	1.0	0.0	0.4	-3.9	-1.7	-0.9	-0.2	0.0	0.0	-12.8
1500.0	$6.50{\cdot}10^{-1}$	0.012	30.9	19.0	8.8	1.0	0.0	0.8	-7.6	-6.0	-1.0	-0.4	0.0	0.0	13.6
2000.0	$3.20{\cdot}10^{-2}$	0.586	8.3	3.4	3.1	1.1	0.0	0.4	-0.4	-0.1	0.5	-0.2	-0.4	0.0	0.6
2000.0	$5.00{\cdot}10^{-2}$	0.476	7.4	2.0	1.4	1.0	0.0	0.3	-0.8	0.1	0.0	0.1	-0.2	0.0	-0.4
2000.0	$8.00{\cdot}10^{-2}$	0.444	7.1	2.0	1.1	1.0	0.0	0.3	-0.3	0.8	-0.6	0.1	-0.1	0.0	0.8
2000.0	$1.30{\cdot}10^{-1}$	0.340	8.3	3.9	1.9	1.0	0.0	0.3	-0.6	0.4	-0.4	-0.1	0.0	0.0	-3.1
2000.0	$1.80{\cdot}10^{-1}$	0.282	9.1	2.6	1.8	1.0	0.0	0.4	-1.2	-0.7	0.1	-0.1	0.0	0.0	-0.5
2000.0	$2.50{\cdot}10^{-1}$	0.234	10.4	5.3	2.3	1.0	0.0	0.4	-0.9	-0.4	-0.2	0.1	0.0	0.0	4.5
2000.0	$4.00{\cdot}10^{-1}$	0.170	13.8	10.1	2.0	1.0	0.0	-0.2	-4.0	-2.5	-0.5	-0.2	0.0	0.0	-8.6
3000.0	$5.00{\cdot}10^{-2}$	0.542	8.7	2.1	1.6	1.0	0.0	0.1	0.9	-0.1	0.4	-0.2	0.2	0.0	-0.1
3000.0	$8.00{\cdot}10^{-2}$	0.438	8.5	2.2	0.8	1.0	0.0	0.3	-0.4	-0.1	-0.3	0.0	-0.2	0.0	-1.6
3000.0	$1.30{\cdot}10^{-1}$	0.325	13.9	4.4	1.4	1.0	0.0	0.3	0.6	1.3	-1.0	-0.1	0.0	0.0	3.7
3000.0	$1.80{\cdot}10^{-1}$	0.243	11.7	3.8	1.4	1.0	0.0	0.3	-1.0	-0.5	-0.1	0.1	0.0	0.0	-3.1
3000.0	$2.50{\cdot}10^{-1}$	0.193	17.7	4.2	2.2	1.0	0.0	-0.2	-1.3	-0.5	-0.1	-0.2	0.7	0.0	-3.1
3000.0	$4.00{\cdot}10^{-1}$	0.089	21.7	9.1	6.7	1.0	0.0	0.5	-4.3	-1.3	-0.6	0.4	0.0	0.0	4.1
3000.0	$6.50{\cdot}10^{-1}$	0.016	33.9	15.3	8.1	1.0	0.0	-0.1	-10.8	-7.0	-0.7	-0.2	0.0	0.0	1.1
5000.0	$8.00{\cdot}10^{-2}$	0.376	9.0	2.7	2.2	1.0	0.0	0.2	-0.9	0.0	0.5	0.0	0.1	0.6	0.0
5000.0	$1.30{\cdot}10^{-1}$	0.284	11.7	2.0	0.8	1.0	0.0	0.4	1.3	0.6	-0.6	0.0	0.0	0.0	0.3
5000.0	$1.80{\cdot}10^{-1}$	0.278	11.3	5.2	2.4	1.0	0.0	0.1	-0.7	0.3	-0.5	0.1	0.0	0.0	4.4
5000.0	$2.50{\cdot}10^{-1}$	0.223	13.2	3.5	2.6	1.0	0.0	0.2	-2.1	0.5	0.1	-0.2	0.0	0.0	0.1
5000.0	$4.00{\cdot}10^{-1}$	0.126	18.3	5.4	1.6	1.0	0.0	-0.3	-2.9	-1.6	-0.3	0.3	0.0	0.0	-3.8
8000.0	$1.30{\cdot}10^{-1}$	0.241	14.5	4.2	4.0	1.0	0.0	0.3	-0.7	-0.1	-0.1	0.0	0.0	0.0	0.0
8000.0	$1.80{\cdot}10^{-1}$	0.272	15.4	5.6	3.6	1.0	0.0	0.3	-0.5	1.0	-0.8	-0.1	0.0	0.0	4.0
8000.0	$2.50{\cdot}10^{-1}$	0.199	18.1	10.8	0.6	1.0	0.0	0.5	-1.6	-0.9	-0.1	0.1	0.0	0.0	-10.6
8000.0	$4.00{\cdot}10^{-1}$	0.119	23.8	6.8	0.8	1.0	0.0	-0.2	-4.1	-1.6	-0.4	-0.2	0.0	0.0	5.0
8000.0	$6.50{\cdot}10^{-1}$	0.036	30.6	14.2	5.7	1.0	0.0	-0.6	-8.1	-4.1	-0.2	0.1	0.0	0.0	-9.1
12000.0	$1.80{\cdot}10^{-1}$	0.238	20.1	3.7	3.1	1.0	0.0	0.2	-1.7	0.2	0.3	0.1	0.0	0.0	0.1
12000.0	$2.50{\cdot}10^{-1}$	0.172	25.9	4.1	3.7	1.0	0.0	0.1	-0.6	0.4	-0.3	-0.1	0.0	0.0	1.2
12000.0	$4.00{\cdot}10^{-1}$	0.084	38.0	3.3	0.8	1.0	0.0	0.5	-2.7	-1.2	0.0	-0.1	0.0	0.0	0.5
20000.0	$2.50{\cdot}10^{-1}$	0.161	35.4	5.2	4.8	1.0	0.0	0.7	-1.5	0.0	0.1	0.0	0.0	0.0	-0.1
20000.0	$4.00{\cdot}10^{-1}$	0.080	$^{+79}_{-48}$	13.9	12.6	1.0	0.0	-0.5	-4.7	-1.4	-0.5	-0.1	0.0	0.0	-3.0
30000.0	$4.00{\cdot}10^{-1}$	0.039	$^{+230}_{-83}$	6.8	4.6	1.0	0.0	0.5	-4.9	-0.4	0.2	0.0	0.0	0.0	-0.6

{9} background subtractions.
As described above, the photoproduction background estimated using the PYTHIA MC simulation agreed with the photoproduction contribution extracted from events tagged by the positron tagger. Uncertainties in the positron-tagger efficiency and in the fake-positron background in the PYTHIA MC simulation led to an overall uncertainty in the photoproduction background of ±35%, as is indicated in Fig.4b. This resulted in an uncertainty in F_2^{em} which is at most 11% for $y \gtrsim 0.4$ and negligible elsewhere;

{10} hadronic energy flow - B.
The hadronic angle $\gamma_{\rm PT}$ was calculated using the energy and angle of hadronic clusters (see Sect. 5). The hadronic angle can lie inside the forward beamhole for low-y events, since the energy deposits around the beamhole are merged into one cluster. To estimate the uncertainty in the cluster algorithm and the simulation of the hadronic final state in the forward direction, a summation over energy deposits in calorimeter cells, instead of EFOs, was used in the hadronic reconstruction. Systematic variations in F_2^{em} up to 10% were observed in the lowest W bins, leaving F_2^{em} at medium and high y unchanged.

The four uncorrelated systematic uncertainties are:

1) positron finding and efficiency.
Varying the isolation criterion requirement of 5 GeV by ±1 GeV around an $\eta - \phi$ cone of radius 0.8 centred on the positron had a negligible effect on F_2^{em};
2) positron scattering angle.
Enlarging the box cut, discussed in Sect. 9.1, by 1 cm in both data and MC simulation had an effect of ±1-3% on F_2^{em} for low values of $Q^2 \lesssim 10$ GeV^2 and a negligible effect elsewhere;

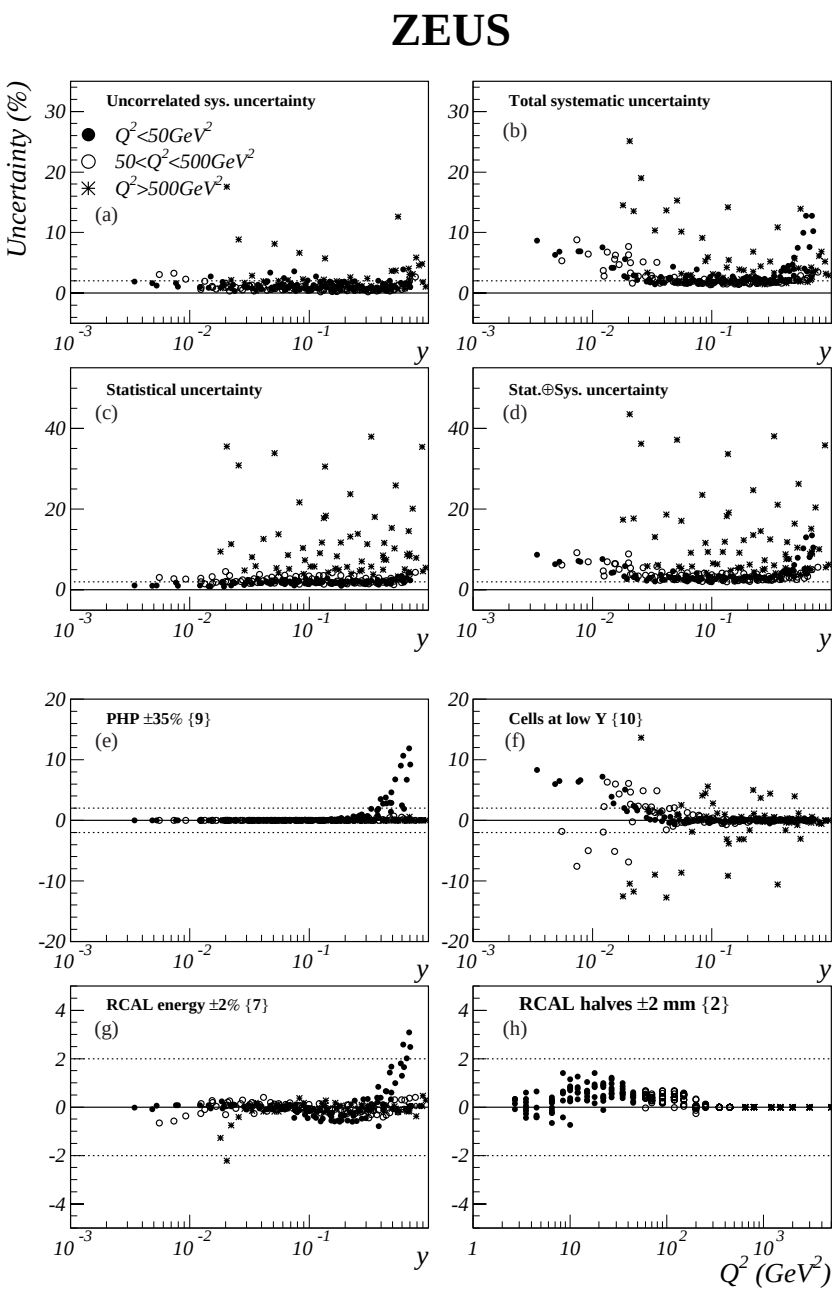

Fig. 7. a–d The relative uncorrelated systematic, total systematic, statistical, and total systematic uncertainty. Three regions in Q^2 are denoted by different symbols. **e–h** Four typical sources of the correlated systematic uncertainty, where the number in {} corresponds to the number in Sect. 10.2. The dotted lines are at ±2%

3) hadronic energy flow - A.
The value of $\gamma_{\max}$ (see Sect. 8) was varied by $\pm 10^\circ$, hence varying the amount of hadronic energy removed from the event. Only small variations in the bias of δ_h were seen in the MC simulation. This reflects the uncertainty in the MC simulation of low-energy deposits in the CAL and the albedo effect. Variations of up to 2% in F_2^{em} were observed in the bins at $y \lesssim 0.02$; elsewhere the variations were within 1%. In the low statistics bins at $x = 0.65$ and $Q^2 > 1200$ GeV^2, this effect increased to $\sim 10\%$;
4) hadronic energy flow - B.
The fraction of events removed by the $P_{T,h}/P_{T,e}$ cut is sensitive to the amount of $P_{T,h}$ lost in the forward beampipe and thus to the details of the jet and proton-remnant fragmentation. The $P_{T,h}/P_{T,e}$ cut was varied from 0.3 by ±0.1, which resulted in changes of 1% at low y.

The systematic uncertainties that did not exhibit a clear correlation were added in quadrature and are listed in Table 2 as δ_{unc}.

The satellite bunches were varied in the MC simulation by ±30% to estimate the uncertainty in the luminosity corresponding to the events in the satellite bunch. Effects on the measured F_2^{em} were typically 0.5-1% and were included in the normalisation uncertainty.

Both the uncorrelated and correlated contributions to the systematic uncertainty were symmetrised by averaging the positive and negative deviations. For the asymmetric

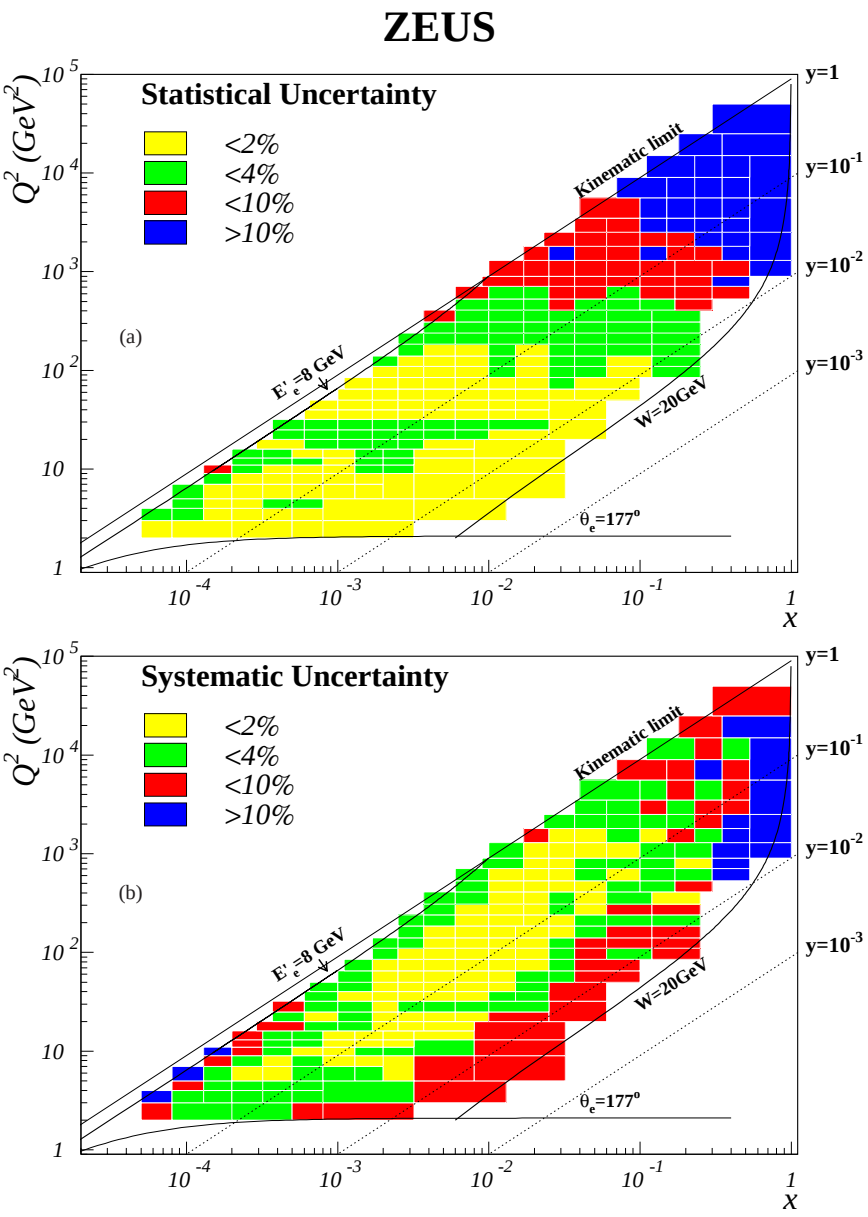

Fig. 8. **a** The statistical uncertainty on F_2^{em}. **b** The systematic uncertainty. Over a large region of phase space both the statistical and systematic uncertainties are below 2%. At the edges of the measurable region the systematic uncertainty increases to $\sim$ 10%. For $y \gtrsim 0.5$, the uncertainty increases due to the uncertainty on the photoproduction background, whereas for $y \lesssim 0.01$ the uncertainty increases mainly because of uncertainties on the hadronic energy flow

systematic checks, such as the boxcut and the check on the clustering, where only a variation in one direction was applied, the variation of the F_2^{em} measurement was symmetrised by mirroring the variation.

Figure 7 shows the statistical and systematic uncertainties on F_2^{em} for each bin as a function of y. Four contributions to the correlated systematic uncertainty are also shown. The two largest contributions to the correlated systematic uncertainty come from {9} and {10}. Most sources of the systematic uncertainty show a correlation between the points as a function of y. The variation of the gap between the two RCAL halves shows a correlation in Q^2. Figure 8 shows the statistical and total systematic uncertainty in each individual bin in the (x, Q^2)-plane.

The systematic uncertainties presented above do not include the uncertainty in the measurement of the integrated luminosity ($\pm 1.5\,\%$), the overall trigger efficiency ($\pm 1.0\,\%$), the higher-order electroweak radiative corrections ($\pm 0.5\%$) or the determination of the vertex distribution ($\pm 1.0\%$). These effects lead to a combined uncertainty of $\pm 2\%$ on the overall normalisation of F_2^{em}. An additional $\pm 1\%$ relative normalisation uncertainty was assigned to the low-Q^2 sample to account for the additional uncertainty on the shape of the vertex distribution in the MC simulation.

10.3 Reduced cross section and F_2^{em}

The values of the reduced cross section, $\tilde{\sigma}^{e^+p}$, and the electromagnetic structure function, F_2^{em}, are given in Table 1 together with their statistical (δ_{stat}) and systematic (δ_{sys}) uncertainties, the corrections due to the Z^0 contribution to F_2, Δ_{F_2}, to the parity-violating component of

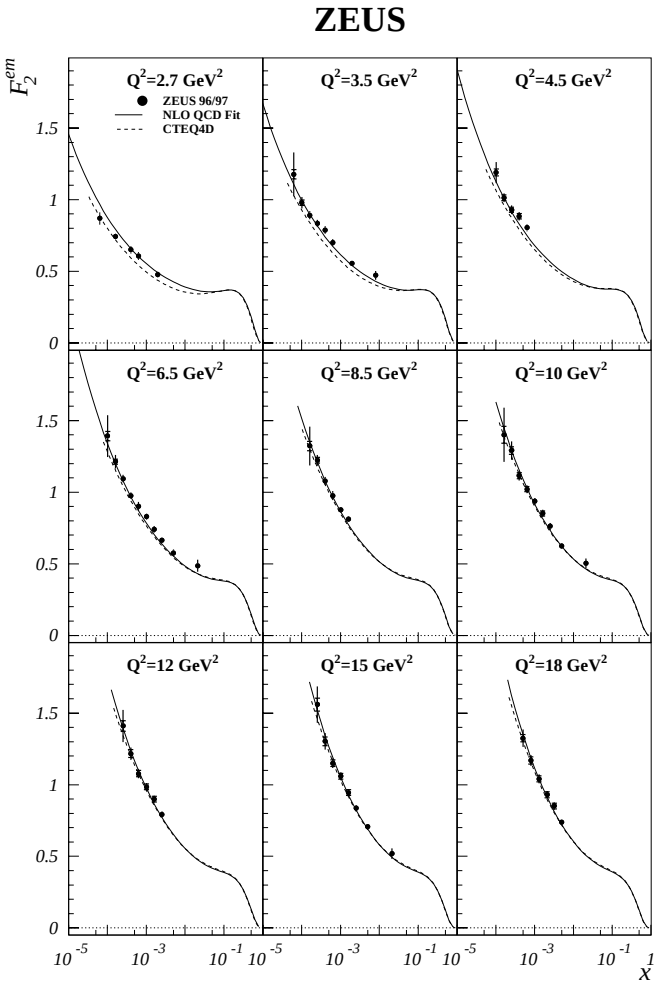

Fig. 9. The results for F_2^{em} (points) are shown versus x for fixed Q^2. The full curves show results from the ZEUS NLO QCD fit and the dashed curves show predictions from CTEQ4D. The inner error bars (delimited by the horizontal lines) show the statistical uncertainties; the outer ones show the statistical and systematic uncertainties added in quadrature. The overall normalisation uncertainties, see Sect. 10.2, are not included

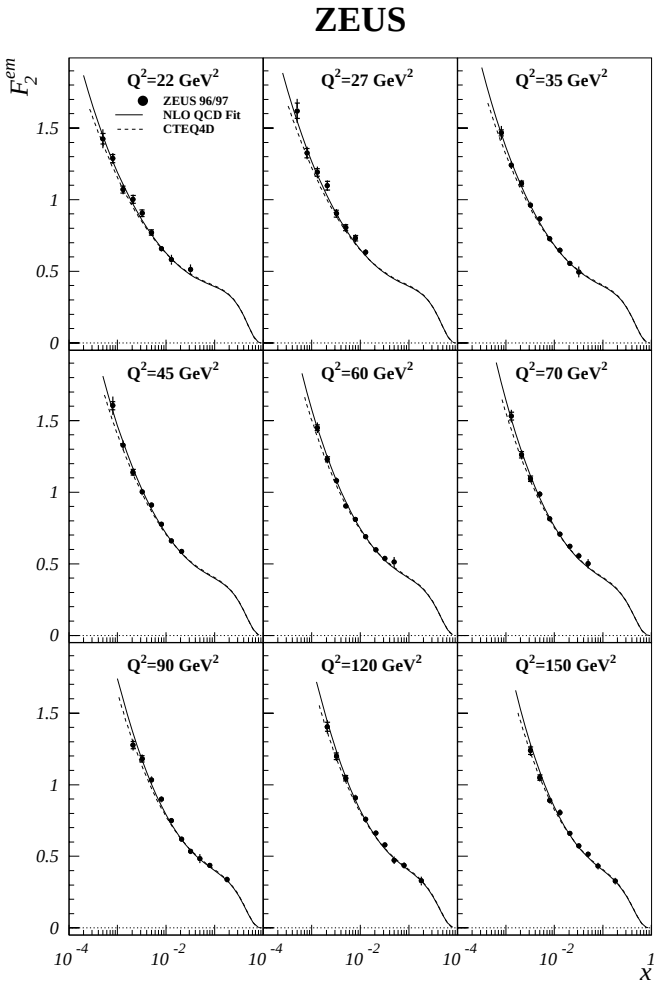

Fig. 10. The results for F_2^{em} (points) are shown versus x for fixed Q^2. For details, see caption of Fig. 9

the Z^0 exchange, Δ_{xF_3}, and to the longitudinal structure function, Δ_{F_L}, see (7)[3]. The contribution of F_L to $\tilde{\sigma}^{e^+p}$ becomes large towards large values of y; the contribution of Z^0 exchange is substantial at large Q^2.

The F_2^{em} values are displayed versus x for fixed values of Q^2 in Figs. 9–12. The structure function is measured with much improved precision with respect to the previous ZEUS results [1]. Also shown is the result of the ZEUS NLO QCD fit described below.

Figures 13 and 14 show the F_2^{em} values as a function of Q^2 for fixed x. Scaling violations are observed, which decrease as x increases. Where the data from the measurements presented here at high x overlap the x range covered by fixed-target experiments [36–38], the agreement is good, as shown in Fig. 14. The results also agree well with the recently published data of the H1 collaboration [2,3] and with the recent parameterisations from CTEQ [39] and MRST [40].

The Q^2-range has increased substantially with respect to previous ZEUS measurements. The ZEUS data in combination with fixed-target data now span almost four orders of magnitude in Q^2 at $x \sim 0.4$.

10.4 NLO QCD fit

A next-to-leading-order (NLO) QCD fit to the reduced cross section from this analysis has been performed. Apart from the present data, proton-target data from NMC [36], BCDMS [37], and E665 [38] were used. Deuteron-target data were used from NMC [36] and E665 [38], as well as data on the ratio F_2^n/F_2^p from NMC [41]. The only neutrino results included in the fit are xF_3 data from CCFR [42].

To remain in the kinematic region where pQCD should be applicable, only data with $Q^2 > 2.5$ GeV^2 were included in the fit. The resonance region and the region

[3] The table with the results and the uncertainities can be obtained from: `http://www-zeus.desy.de/publications.php3`

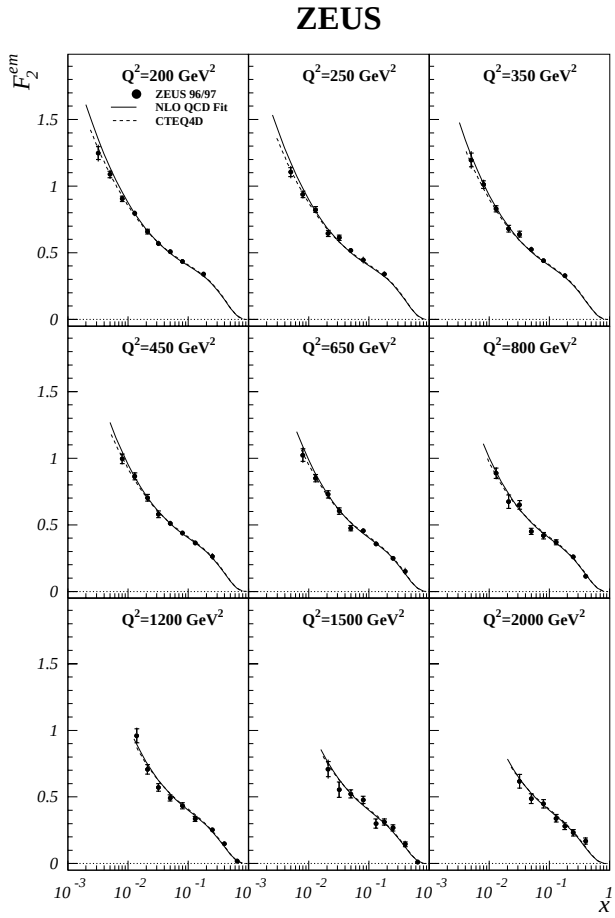

Fig. 11. The results for F_2^{em} (points) are shown versus x for fixed Q^2. For details, see caption of Fig. 9

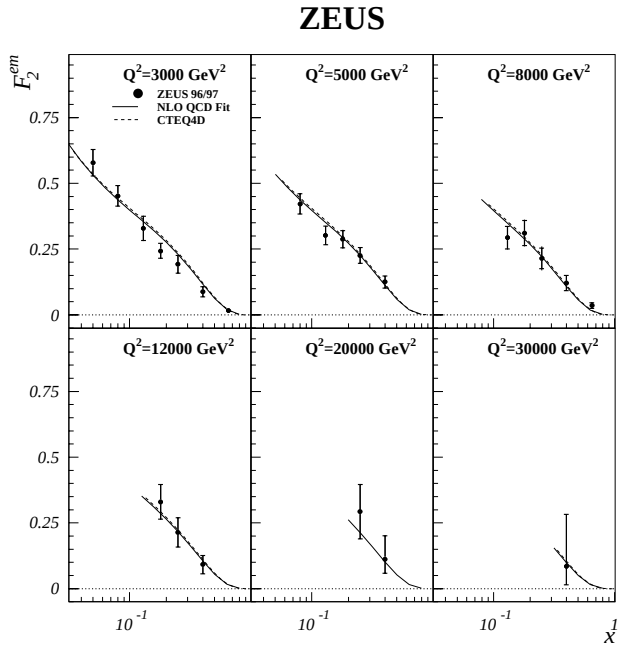

Fig. 12. The results for F_2^{em} (points) are shown versus x for fixed Q^2. For details, see caption of Fig. 9

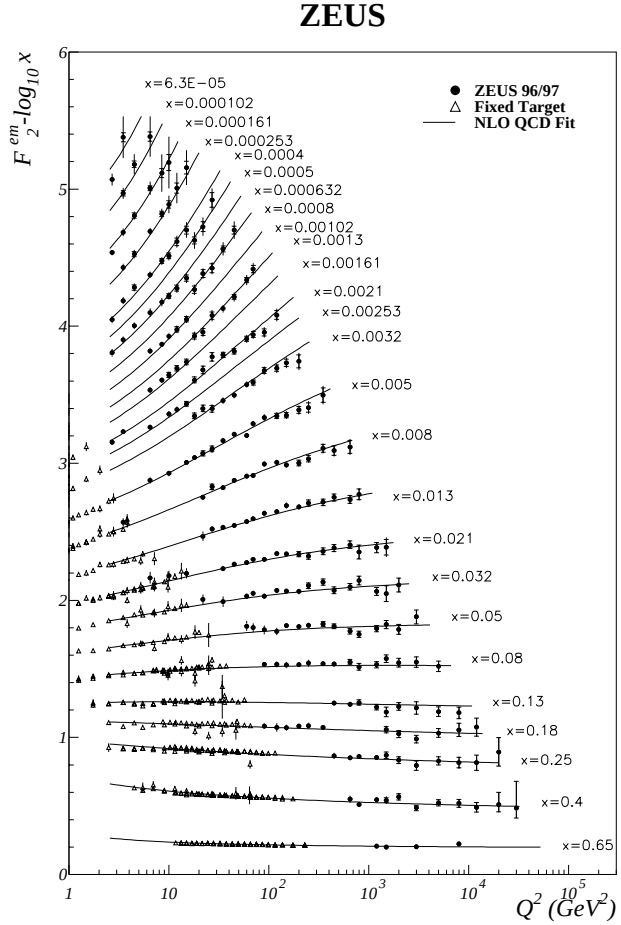

Fig. 13. The results for F_2^{em} (points) versus Q^2 are shown for fixed x. The fixed-target results from NMC, BCDMS and E665 (triangles) and the ZEUS NLO QCD fit (curve) are also shown

affected by higher-twist contributions and target-mass effects ($x \gtrsim 0.1$, $Q^2 \lesssim 20$ GeV^2) were avoided by requiring $W^2 > 20$ GeV^2.

The parameterisations of the parton density functions (PDFs) were assumed to have the following functional form, adapted from MRST [40]:

$$xf(x, Q_0^2) = Ax^{\delta}(1-x)^{\eta}(1+\gamma x)$$

and were evaluated at $Q_0^2 = 7$ GeV^2. The x^{δ} term parameterises the steep rise at low x, whereas $(1-x)^{\eta}$ describes the shape of the valence quarks at high x.

The fit was done in the $\overline{\rm MS}$ scheme with a variable-flavour-number *ansatz* (RT-VFN) [43]. A charm mass of 1.35 GeV was assumed. The strange-quark distribution, $x(s(x) + \bar{s}(x)) = 2x\bar{s}(x)$, was fixed to the world-average value 0.20 of the total sea, according to measurements of CCFR [44]. The value of α_S was fixed to the world average value, $\alpha_S(M_Z^2) = 0.118$.

The QCD NLO fit reproduces the data over the full kinematic range, indicating that NLO DGLAP evolution can give a consistent description. The overall χ^2/ndf of the fit is 0.95 for 1263 data points, where the χ^2 is calculated using the statistical and total systematic uncertainty added in quadrature. The χ^2/ndf for the present data is 0.84 for the 242 ZEUS data points.

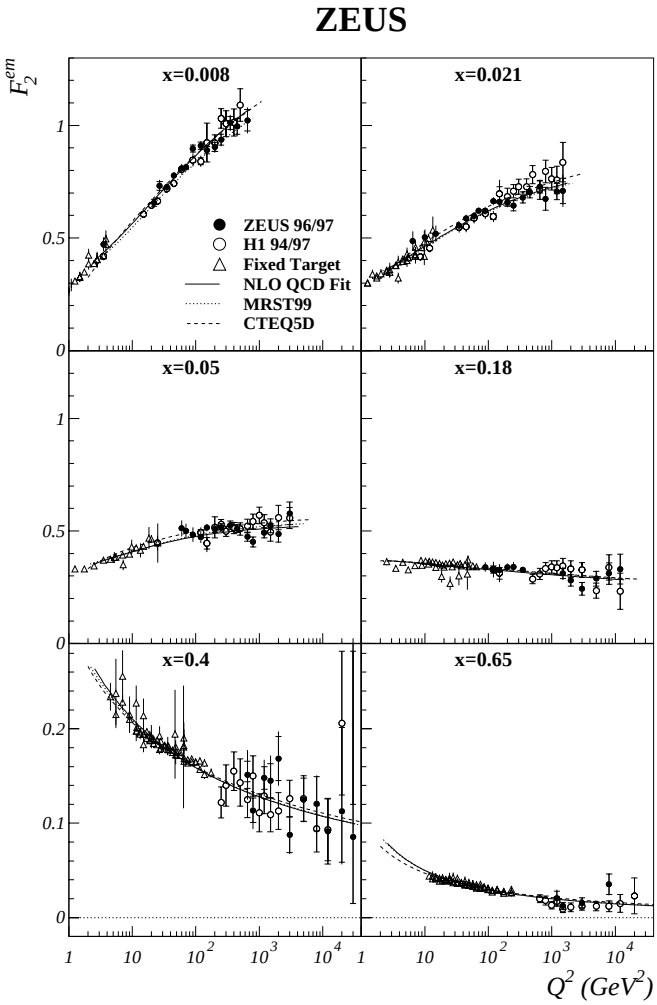

Fig. 14. The results for F_2^{em} versus Q^2, for six bins at fixed x, are compared with results from NMC, BCDMS, E665 (triangles) and the recently published H1 results (open symbols). The inner error bars (delimited by the horizontal lines) show the statistical uncertainties; the outer ones show the statistical and systematic uncertainties added in quadrature, both for ZEUS and H1

11 Conclusions

Measurements of the reduced cross section and the proton structure function, F_2^{em} , have been presented from an analysis of inelastic positron-proton neutral current scattering data. The data were taken with the ZEUS detector at HERA during 1996 and 1997. The structure function F_2^{em} has now been measured over a substantially larger phase space than covered by previous ZEUS measurements and with statistical and systematic uncertainties below 2% in most of the (x, Q^2) region covered. The data cover Q^2 values between 2.7 and 30000 GeV^2 and x values between $6 \cdot 10^{-5}$ and 0.65.

At large x values and Q^2 values up to 70 GeV^2, where the new data reach the x-range covered by fixed-target experiments, good agreement with these experiments is found. There is also good agreement with the data of the H1 collaboration. Strong scaling violations are observed for $x < 0.02$. The measured x-Q^2 behaviour of F_2^{em} can be described by QCD using NLO DGLAP evolution over the full kinematic range.

Acknowledgements. The strong support and encouragement of the DESY Directorate has been invaluable. The experiment was made possible by the inventiveness and the diligent efforts of the HERA machine group. The design, construction and installation of the ZEUS detector have been made possible by the ingenuity and dedicated efforts of many people from inside DESY and from the home institutes who are not listed as authors. Their contributions are acknowledged with great appreciation. Useful conversations with H. Spiesberger and R. Thorne are also gratefully acknowledged.

References

1. ZEUS Collab., M. Derrick et al., Z. Phys. **C 72**, 399 (1996)
2. H1 Collab., C. Adloff et al., Eur. Phys. J. **C 13**, 609 (2000)
3. H1 Collab., C. Adloff et al., Preprint DESY-00-181 (hep-ex/0012053), 2000. Accepted by Eur. Phys. J. C
4. Particle Data Group, D.E. Groom et al., Eur. Phys. J. **C15**, 73 (2000)
5. J. Blümlein and M. Klein, in *Proc. Workshop on Physics at HERA, Oct. 1991*, eds. W. Buchmüller and G. Ingelman, Vol. 1, p. 101. Hamburg, Germany, DESY, 1992
6. M. Derrick et al., Nucl. Instr. and Meth. **A 309**, 77 (1991) A. Andresen et al., Nucl. Instr. and Meth. **A 309**, 101 (1991) A. Caldwell et al., Nucl. Instr. and Meth. **A 321**, 356 (1992) A. Bernstein et al., Nucl. Instr. and Meth. **A 336**, 23 (1993)
7. A. Bamberger et al., Nucl. Instr. and Meth. **A 382**, 419 (1996)
8. N. Harnew et al., Nucl. Instr. and Meth. **A 279**, 290 (1989) B. Foster et al., Nucl. Phys. Proc. Suppl. **B 32**, 181 (1993) B. Foster et al., Nucl. Instr. and Meth. **A 338**, 254 (1994)
9. ZEUS Collab., U. Holm (ed.), *The ZEUS Detector*, Status Report, (unpublished), DESY, 1993, available on `http://www-zeus.desy.de/bluebook/bluebook.html`
10. A. Bamberger et al., Nucl. Instr. and Meth. **A 401**, 63 (1997)
11. J. Andruszków et al., Report DESY-92-066, DESY, 1992 ZEUS Collab., M. Derrick et al., Z. Phys. **C 63**, 391 (1994)
12. W.H. Smith et al., Nucl. Instr. and Meth. **A 355**, 278 (1995)
13. U. Bassler and G. Bernardi, Nucl. Instr. and Meth. **A 361**, 197 (1995)
14. R. Brun et al., GEANT3, Technical Report CERN-DD/EE/84-1, CERN, 1987
15. A. Kwiatkowski, H. Spiesberger and H.-J. Möhring, Comp. Phys. Comm. **69**, 155 (1992). Also in *Proc. Workshop Physics at HERA*, 1991, DESY, Hamburg
16. G. Ingelman, A. Edin and J. Rathsman, Comp. Phys. Comm. **101**, 108 (1997)
17. K. Charchula, G.A. Schuler and H. Spiesberger, Comp. Phys. Comm. **81**, 381 (1994)
18. Y. Azimov et al., Phys. Lett. **B 165**, 147 (1985) G. Gustafson and U. Petterson, Nucl. Phys. **B306**, 746 (1988)
19. B. Andersson et al., Z. Phys. **C 43**, 625 (1989)

20. L. Lönnblad, Comp. Phys. Comm. **71**, 15 (1992)
21. T. Sjöstrand, Comp. Phys. Comm. **82**, 74 (1994)
22. ZEUS Collab., J. Breitweg et al., Eur. Phys. J. **C 6**, 239 (1999)
23. ZEUS Collab., J. Breitweg et al., Eur. Phys. J. **C 6**, 43 (1999)
24. H1 Collab., C. Adloff et al., Z. Phys. **C 76**, 613 (1997)
25. H. Jung, Comp. Phys. Comm. **86**, 147 (1995)
26. H.L. Lai et al., Phys. Rev. **D 51**, 4763 (1995)
27. ZEUS Collab., J. Breitweg et al., Eur. Phys. J. **C 1**, 109 (1998)
28. H. Abramowicz et al., Phys. Lett. **B 269**, 465 (1991)
29. H. Abramowicz, A. Caldwell and R. Sinkus, Nucl. Instr. and Meth. **A 365**, 508 (1995)
30. ZEUS Collab., J. Breitweg et al., Eur. Phys. J. **C 11**, 427 (1999)
31. F. Jacquet and A. Blondel, in *Proceedings of the Study for an ep Facility for Europe*, ed. U. Amaldi, p. 391. Hamburg, Germany, 1979. Also in preprint DESY 79/48
32. S. Bentvelsen, J. Engelen and P. Kooijman, in *Proc. Workshop on Physics at HERA, Oct. 1991*, eds. W. Buchmüller and G. Ingelman, Vol. 1, p. 23. Hamburg, Germany, DESY, 1992 K.C. Höger, *Measurement of x, y and Q^2 in neutral current events.* Ibid, p.43
33. N. Tuning, *Proton structure functions at HERA*. Ph.D. Thesis, University of Amsterdam, 2001, available on `http://www.nikhef.nl/pub/services/library.html`
34. H.L. Lai et al., Phys. Rev. **D 55**, 1280 (1997)
35. A. Arbuzov et al., Comp. Phys. Comm. **94**, 128 (1996)
36. NMC Collab., M. Arneodo et al., Nucl. Phys. **B 483**, 3 (1997)
37. BCDMS Collab., A.C. Benvenuti et al., Phys. Lett. **B 223**, 485 (1989)
38. E665 Collab., M.R. Adams et al., Phys. Rev. **D 54**, 3006 (1996)
39. CTEQ Collab., H.L. Lai et al., Eur. Phys. J. **C 12**, 375 (2000)
40. A.D. Martin et al., Eur. Phys. J. **C 14**, 133 (2000)
41. NMC Collab., M. Arneodo et al., Nucl. Phys. **B 487**, 3 (1997)
42. CCFR Collab., E. Oltman et al., Z. Phys. **C 53**, 51 (1992)
43. R.S. Thorne and R.G. Roberts, Phys. Rev. **D 57**, 1998 (1998) R.S. Thorne and R.G. Roberts, Phys. Lett. **B 421**, 303 (1998)
44. CCFR Collab., A.O. Bazarko et al., Z. Phys. **C65**, 189 (1995)